Experimental validation of a rate-dependent Data-Driven stress Identification method

Adrien Vinel, Rian Seghir, Julien Berthe, Gerald Portemont, Julien Réthoré

Received: Added at production | Revised: Added at production | Accepted: Added at production

DOI: xxx/xxxx

FULL PAPER

Experimental validation of a rate-dependent Data-Driven stress Identification method

Adrien Vinel[1,2] | Rian Seghir[1] | Julien Berthe[2] | Gérald Portemont[2] | Julien Réthoré[1]

[1]GeM, Centrale Nantes, UMR 6183 CNRS, Nantes, France
[2]DMAS, ONERA, F-59014 Lille, France

Correspondence
Julien Réthoré, GeM, Centrale Nantes, France. Email: julien.rethore@ec-nantes.fr

Abstract

Document de travail

KEYWORDS:

1 | INTRODUCTION

Recently, several strategies have been adopted to estimate stress fields in non-standard experiments without using a constitutive law. These strategies all rely on full-field measurements and a regularization of the ill-posed mechanical problem, but differ on the chosen regularization.

In 2014, Pierron and his co-authors [28] devised a strategy to estimate stress fields in dynamics without using a constitutive law. To this effect, the strategy relies on the use of a statically determined configuration (an inertial impact test for instance). Under the assumptions of plane stress, and a homogeneous and constant density of the material, the authors are able to estimate the mean stress field profile in the specimen. For this strategy, the acceleration acquired experimentally acts as a load cell, which requires recording kinematic fields at ultra-high speed ($\geq$ 1M fps). This work opened the way to the so called Image-Based Inertial Impact Tests (IBII). Among other, it allowed the authors to identify the elastic modulus and tensile strength of tungsten carbide cermets [8] and a composite [10] at high strain-rate. More recently, the strategy was also applied in a new experimental configuration: the Image-Based Inertial Release (IBIR) test [9]. This new configuration allowed the identification of both quasi-static and high strain-rate elastic modulus and Poisson's ratio for PMMA. In these examples, the boundary conditions (purely inertial test and uniaxial) regularize the problem. If the test is not uniaxial any more, the authors proposed an elegant solution in the case of elastic orthotropic material [27].

Even more recently, in 2021, Liu *et al.* [24] and Cameron and his co-author [3] devised another strategy to estimate stress fields without postulating a constitutive equation. Assuming that the material is isotropic, the methods developed by these authors rely on the alignment of the principal directions of stress with strain or strain-rate. This assumption then allows obtaining a mathematically closed problem, and thus the analytical estimation of stresses. These methods have been tested on numerical example and experimentally in [24]. In [3], the authors discuss the range of validity of such an assumption: mainly in isotropic elasticity, plasticity with associative flow rules and for associative flow rules with an isotropic yield function. Furthermore, this method cannot address the problem of elasto-plastic transition where stresses are not aligned with strains anymore and not aligned with plastic strain-rates yet.

The recent developments in computer science and in particular in the data science field, has lead to the emergence of a third kind of strategy relying on data in the past 4 years: the so called Data-Driven approaches. These methods can be used to either solve the direct problem [14] or the inverse mechanical problem [22]. The so called Data-Driven methods were first introduced in the context of computational mechanics by Kirchdoerfer and Ortiz [14, 15]. In their work, the authors replaced the constitutive equation by a minimization process and a material database. A solution is found by minimizing a distance (which they defined) between computed mechanical states (strains and stresses) and a set of admissible material states. The authors then extended their methods to dynamics [16]. These methods called Data-Driven Computational Mechanics are used to solve the direct problem: find the response of structure (strains and stresses) using a set of

admissible material states, which have to be found experimentally. These works were then derived in order to formulate inverse Data-Driven approaches. Hence, in their work Leygue and his co-authors [22, 23] formulated the inverse problem associated to the Data-Driven Computational Mechanics. This new problem aims to estimate stress fields from heterogeneous experiments without having to explicit any constitutive equation. Using synthetic data, the authors demonstrated the ability of their algorithm to estimate admissible stresses in a structure for various loading cases (quasi-static and dynamic problems) as well as different material behaviours (hyperelasticity, elasto-plastiticy). This Data-Driven method was then applied to experimental data by Dalémat *et al.* in [5]. In this study, perforated hyperelastic membranes are submitted to uniaxial tensile tests. In addition, in a recent paper [4] extensively discuss the proper way to handle imperfect experimental data. The authors especially discuss the boundary conditions for imperfectly defined edges and the way to tackle the issue of missing data. More recently, the Data-Driven strategy was applied by Langlois and his co-authors to experiments on history dependent materials [**?**]. The use of this method enabled them to estimate stress fields for an elasto-platic material that is subjected to the formation of Piobert-Lüders bands. In these strategies, the regularization comes from the assumption that the material response lies on a manifold in a constitutive space which remains to be determined. The underlying hypothesis of this method will be presented later-on in this paper. Furthermore, one could imagine combining this method with the IBII method in order to estimate heterogeneous 2D stress fields in dynamics without needing load measurements.

These emergent strategies can potentially help to assess, without making any assumptions, the validity of material constitutive equations outside their validity domain (*e.g.* heterogeneous tests, with multi-axiality, couplings...). In that context, the Data-Driven Identification formulation and resolution strategy for visco-elasto-plastic materials will first be recalled. Then, a digital twin is built to investigate the ability of such a method to estimate stress fields, and especially its accuracy. At last but not least, the DDI is then applied to data obtained during a high speed tensile test performed on a heterogeneous sample made in steel.

2 | DATA-DRIVEN IDENTIFICATION METHOD

The inverse Data-Driven Identification method requires both, a rich database of displacement fields (obtained for example with DIC on complex sample geometries), and net external forces (usually obtained with a load cell). Combined with conservation laws (balance of linear and angular momentum), valid whatever the material, it is possible to build a minimization problem where the components of stress fields are the sought parameters. The following section guides the reader up to final formulation of the global minimization problem.

To make the implementation clearer, we use in the following only matrix notation instead of tensorial one. By default, we use $[\bullet]$ for matrices and $\{\bullet\}$ for vectors. When indices are explicitly required they are emphasized as followed, X_i^j, where i and j are matrix rows and columns respectively.

While the main ingredients are recalled in detail we refer interested readers to [22] where the *DDI* problem was originally introduced. This work is also inspired by the works of Eggersmann and his co-authors [6] where the framework was extended for history dependent materials. Furthermore, the modified strategy, regarding the initialization of the problem, proposed in [23] is adopted. Some notations that will be recalled and used in this work was introduced by Langlois and his co-authors in [18]. The problem is formulated here in small strain, however it has already been implemented and used in finite strain in [5, 29]. Moreover, for experimental concerns, we will focus only on plane-stress formalism.

2.1 | Static equilibrium problem

The general problem considers a 2D structure made of a deformable material (see Fig. 1). This structure is discretized

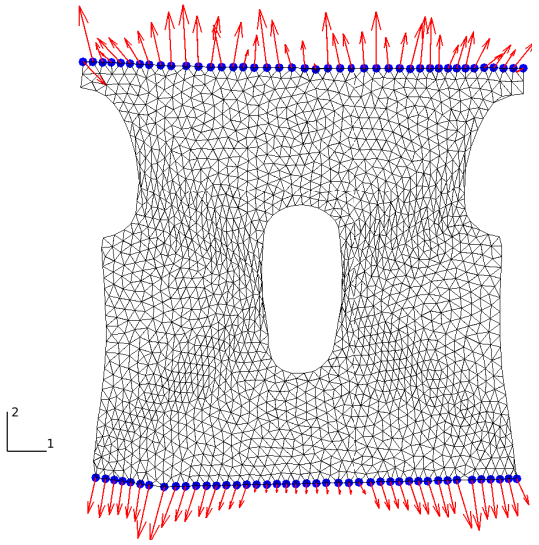

FIGURE 1 2D deformable structure made of T3P1 elements over a domain Ω. Blue bullets define the border ∂F where loads and / or displacements are prescribed. Red arrows show a distribution of reaction forces.

using a Finite Element mesh with N_e elements and N_n nodes and the loading is discretized through N_t time steps.

Available data are the following:

- $[u]$: a $2N_n \times N_t$ matrix collecting nodal displacements obtained from DIC over the domaine Ω. The dimension $2N_n$ means that displacement vectors are organized in vector format such as $\left\{u^t\right\} = \left\{u1_1^t, ..., u1_n^t, u2_1^t, ..., u2_n^t\right\}$ where u1 and u2 are transverse and axial displacements respectively (see Fig. 1),

- $[B]$: a $3N_e \times 2N_n$ matrix obtained from the assembly of elementary FEM gradient operators. The dimension $3N_e$ encloses the 3 components of the displacement gradient. It is computed using the geometry, mesh connectivity and relies on triangular elements and classical linear Lagrange shape functions. It allows for computing strain tensors at every quadrature points, here element centroid noted e. They are collected in a $3N_e \times N_t$ matrix:

$$[\boldsymbol{\varepsilon}] = [B]\,[u]\,, \tag{1}$$

- $[w]$: a $3N_e \times 3N_e$ diagonal matrix collecting the elementary integration weights times Jacobian determinants of the transformation of each element from its reference coordinates frame to its actual shape in the global coordinate system,

- $\{F\}$: a N_t vector collecting the net force, along the axial direction 2 (see Fig. 1) of the nodal forces on the boundary ∂F:

$$\{F\} = h \sum_{k \in \partial f} f^t_{N_n+k} \quad \forall t \in [1, N_t] \tag{2}$$

with h the thickness of the structure, supposed to be constant, and $[f]$ a $2N_n \times N_t$ matrix collecting the nodal internal forces. N_n+k refers to axial displacements only.

Static equilibrium can therefore be expressed through a set of N_t systems of $2N_n$ linear equations:

$$\begin{aligned} &[B]^{\mathrm{T}}\,[w]^{\mathrm{T}}\left\{\boldsymbol{\sigma}^t\right\} = \left\{f^t\right\},\ \forall t \in [1, N_t] \\ &\text{with} \sum_{k \in \partial f} f^t_{N_n+k} = \frac{F^t}{h} \text{ and } f^t_k = 0,\ \forall k \in \Omega \backslash \partial F. \end{aligned} \tag{3}$$

Considering boundary conditions, especially the fact that only the net force along the axial direction 2 (see Fig. 1) is usually known in practice, and that displacements are prescribed everywhere else on ∂F, the set of $2N_n$ equations can be reduced to $\hat{N} = 2N_n - 4\,\mathrm{card}(\partial F) + 1$. It is implemented by discarding from the system of equation 3 constrained boundary nodes and by adding the linear combination introduced in Eq. 2. It leads to the definition of news operators $\left[\hat{B}\right]$ and $\left[\hat{f}\right]$ summarizing mechanical equilibrium into a compact form:

$$\left[\hat{B}\right]^{\mathrm{T}}[w]^{\mathrm{T}}\left\{\boldsymbol{\sigma}^t\right\} = \left\{\hat{f}^t\right\},\ \forall t \in [1, N_t]. \tag{4}$$

2.2 | Data-Driven Identification problem

The main idea behind the *DDI* method consists in assuming that a constitutive equation exists, hence there is a constitutive space (still to be defined) where the whole set of mechanical states lies on a manifold. In short, among the infinity of solution of the static problem (see Eq. 4), one seeks for the one that minimizes the spread around an unknown manifold within a well defined constitutive space. Notice that in the following, such a manifold will be approximated by discrete points named material states, in the sense that they literally sample the material response in the constitutive space. Such a discretization allows for regularizing the ill-posed problem of stress identification as we will see later-on.

As a consequence 3 main ingredients have to be defined: (1) such a "well defined" constitutive space, (2) a norm for estimating distances between states in this constitutive space, and (3) the sampling of the manifold. Main assumptions of the method are enclosed in these three ingredients.

Constitutive space has to be chosen wisely regarding the various dependencies of the material response to observable and sought quantities. Following Eggersman *et al.* recommendations [6], the history and time-dependent behaviour of the material will be described using strain, stress and their first order time derivatives. To this effect, similarly to what is done in [18], an incremental approach will be used, leading to a dependence of the current stress to the current strain as well as the former strain and stress.

$$\boldsymbol{\sigma}^t = \hat{\sigma}^t\left(\boldsymbol{\varepsilon}^t, \boldsymbol{\varepsilon}^{t-1}, \boldsymbol{\sigma}^{t-1}\right) \tag{5}$$

$\hat{\sigma}^t$ will be further used as the *DDI* estimation of the actual stress in this particular space. As a result, the constitutive space that will be considered in this work is $\left(\boldsymbol{\varepsilon}^t, \boldsymbol{\varepsilon}^{t-1}, \boldsymbol{\sigma}^t, \boldsymbol{\sigma}^{t-1}\right)$. From a modelling point-of-view, such a differential constitutive space approaches the material response similarly to rate-dependent plasticity models, classically used in high-strain rate simulation like Johnson-Cook models [], which has to be distinguished from visco-plastic models where relaxation time, meaning larger time non-locality, can properly be taken into account.

Then, let us define a distance in a generic strain and stress related constitutive space. Following [14] we choose a norm built from a symmetric positive definite fourth-order tensor $\mathbb{C}_o$. Noting for example $\left\{\mathcal{P}^t\right\}$ and $\left\{\mathcal{Q}^t\right\}$, two vectors related to some strain and stress quantities at time t respectively in Voigt

notation, an energetic $\|\|^2_{\mathbb{C}_o}$ norm can be introduced as follows:

$$\|\mathcal{P}^t, \mathcal{Q}^t\|^2_{\mathbb{C}_o} = \left\{\mathcal{P}^t\right\}^{\mathrm{T}} \left[\mathbb{C}_o\right] \left\{\mathcal{P}^t\right\} + \left\{\mathcal{Q}^t\right\}^{\mathrm{T}} \left[\mathbb{C}_o\right] \left\{\mathcal{Q}^t\right\}. \quad (6)$$

Normalizing data, such as:

$$\begin{aligned} \left\{\underline{\mathcal{P}}^t\right\} &= \left[\sqrt{\mathbb{C}_o}\right] \left\{\mathcal{P}^t\right\}, \\ \left\{\underline{\mathcal{Q}}^t\right\} &= \left[\sqrt{\mathbb{C}_o}\right]^{-1} \left\{\mathcal{Q}^t\right\}, \end{aligned} \quad (7)$$

the norm simply becomes:

$$\|\mathcal{P}^t, \mathcal{Q}^t\|^2_{\mathbb{C}_o} = \left\{\underline{\mathcal{P}}^t\right\}^{\mathrm{T}} \left\{\underline{\mathcal{P}}^t\right\} + \left\{\underline{\mathcal{Q}}^t\right\}^{\mathrm{T}} \left\{\underline{\mathcal{Q}}^t\right\}. \quad (8)$$

Notice that the square root of the tensor $\left[\mathbb{C}_o\right]$ is computed using an Eigen decomposition, $\left[\sqrt{\mathbb{C}_o}\right] = [V]\left[\sqrt{D}\right][V]^{\mathrm{T}}$, where $[V]$ and $[D]$ are matrices containing Eigen vectors and values respectively. Such a normalization will help the clustering part of the problem (see Sec. 2.4).

As introduced above, to address the issue of ill-posness of the stress-field identification problem (infinite dimension of the manifold) the material response is discretized with a finite N^* set of unknown material states $(\{\boldsymbol{\varepsilon}^*\}, \{\boldsymbol{\varepsilon}^{**}\}, \{\boldsymbol{\sigma}^*\}, \{\boldsymbol{\sigma}^{**}\})$, where $\bullet^*$ are related to the current state and $\bullet^{**}$ to the former state. We will see that these N^* states are in practice defined as barycenters of mechanical states clusters. These clusters regroup the set of strains and sought stresses $\left(\left\{\boldsymbol{\varepsilon}^t\right\}, \left\{\boldsymbol{\varepsilon}^{t-1}\right\}, \left\{\boldsymbol{\sigma}^t\right\}, \left\{\boldsymbol{\sigma}^{t-1}\right\}\right)$ that are close in the $\|\|^2_{\mathbb{C}_o}$ norm sense. The following form of the *DDI* method can therefore be seen as a zero-order approach in the sense that the regularization introduced by the material states is piece-wise constant.

Using the constitutive space introduced in Eq. 5, the norm introduced in Eq. 8 and the sampling of the material response into N^* current and former states, the problem can be formulated as a global minimization:

$$\min_{\substack{\boldsymbol{\varepsilon}^*\boldsymbol{\varepsilon}^{**}\hat{\boldsymbol{\sigma}} \\ \boldsymbol{\sigma}^*\boldsymbol{\sigma}^{**}S}} \Psi\left(\boldsymbol{\varepsilon}, \boldsymbol{\varepsilon}^*, \boldsymbol{\varepsilon}^{**}, \hat{\boldsymbol{\sigma}}, \boldsymbol{\sigma}^*, \boldsymbol{\sigma}^{**}, S\right), \quad (9)$$

where

$$\Psi = \frac{1}{2} \sum_{t=2}^{N_t} \left(\|\mathcal{P}^t, \mathcal{Q}^t\|^2_{\mathbb{C}_o} + \|\mathcal{P}^{t-1}, \mathcal{Q}^{t-1}\|^2_{\mathbb{C}_o} \right), \quad (10)$$

with

$$\begin{aligned} \underline{\mathcal{P}}^t &= \left[\sqrt{p^t}\right] \left(\left\{\underline{\boldsymbol{\varepsilon}}^t\right\} - \left[S^t\right] \left\{\underline{\boldsymbol{\varepsilon}}^*\right\}\right), \\ \underline{\mathcal{P}}^{t-1} &= \left[\sqrt{p^{t-1}}\right] \left(\left\{\underline{\boldsymbol{\varepsilon}}^{t-1}\right\} - \left[S^t\right] \left\{\underline{\boldsymbol{\varepsilon}}^{**}\right\}\right), \\ \underline{\mathcal{Q}}^t &= \left[\sqrt{p^t}\right] \left(\left\{\underline{\hat{\boldsymbol{\sigma}}}^t\right\} - \left[S^t\right] \left\{\underline{\boldsymbol{\sigma}}^*\right\}\right), \\ \underline{\mathcal{Q}}^{t-1} &= \left[\sqrt{p^{t-1}}\right] \left(\left\{\underline{\hat{\boldsymbol{\sigma}}}^{t-1}\right\} - \left[S^t\right] \left\{\underline{\boldsymbol{\sigma}}^{**}\right\}\right), \end{aligned} \quad (11)$$

under the constraint that the equilibrium conditions (Eq. 4) are satisfied. $[p]$ is a $3N_e \times 3N_e \times N_t$ matrix weighing mechanical states contributions for every time-steps within the functional Ψ. A specific section (see Sec. 2.5) is dedicated later-on to address the specific role of these weights in the time and space integral. $[S]$ is a $3N_e \times 3N^* \times N_t$ selection matrix that maps the N^* material states to the mechanical states for every time-steps. Eq. 9 must be understood as the global minimization (time and space) of the scattering of mechanical states around their associated N^* material states (piece-wise barycenters) in the particular constitutive space $(\boldsymbol{\varepsilon}^t, \boldsymbol{\varepsilon}^{t-1}, \boldsymbol{\sigma}^t, \boldsymbol{\sigma}^{t-1})$.

If equilibrium constraints are enforced using Lagrange multipliers, the following cost function can be obtained:

$$\Phi = \Psi + \sum_{t=1}^{N_t} \left(\left[\underline{\hat{\boldsymbol{B}}}\right]^{\mathrm{T}} [w]^{\mathrm{T}} \left\{\underline{\hat{\boldsymbol{\sigma}}}^t\right\} - \left\{\hat{f}^t\right\} \right) \left\{\lambda^t\right\} \quad \forall t \in [1, N_t]. \quad (12)$$

Notice that the introduction of normalized quantities "$\underline{\bullet}$" also requires the normalization of $\underline{\hat{\boldsymbol{B}}}$. It is simply done by assembling normalized gradient operators. Finally, two problems can be formulated: (1) the mechanical and (2) the material one. The stationarity of Φ with respect to $\left\{\lambda^t\right\}$ and $\left\{\underline{\hat{\boldsymbol{\sigma}}}^t\right\}$ leads to the mechanical problem and the following set of N_t systems of $3N_e \times \hat{N}$ equations:

$$\begin{bmatrix} \left[\underline{\hat{\boldsymbol{B}}}\right]^{\mathrm{T}} [w]^{\mathrm{T}} & 0 \\ \alpha^t & \left[p^t\right]^{-1} [w] \left[\underline{\hat{\boldsymbol{B}}}\right] \end{bmatrix} \begin{Bmatrix} \underline{\hat{\boldsymbol{\sigma}}}^t \\ \lambda^t \end{Bmatrix} = \begin{Bmatrix} \hat{f}^t \\ D^t \end{Bmatrix} \quad (13)$$

with,

$$\alpha^t = \begin{cases} 1 & \forall t \in [1, N_t], \\ 2 & \forall t \in [2 : N_{t-1}], \end{cases}$$

$$\left\{D^t\right\} = \begin{cases} \left[S^{t+1}\right] \left\{\underline{\boldsymbol{\sigma}}^{**}\right\} & t = 1, \\ \left[S^{t+1}\right] \left\{\underline{\boldsymbol{\sigma}}^{**}\right\} + \left[S^t\right] \left\{\underline{\boldsymbol{\sigma}}^*\right\} & \forall t \in [2 : N_{t-1}], \\ \left[S^t\right] \left\{\underline{\boldsymbol{\sigma}}^*\right\} & t = N_t. \end{cases} \quad (14)$$

One key element to obtain such an expression is to observe the following relations:

Then, the stationarity with respect to the material states leads to the material problem and the following 4 sets of $3N^*$ equations:

$$\begin{cases} \sum_{t=2}^{N_t} \left[\mathcal{M}^{*t}\right] \left[S^t\right] \left\{\underline{\boldsymbol{\varepsilon}}^*\right\} &= \sum_{t=2}^{N_t} \left[\mathcal{M}^{*t}\right] \left\{\underline{\boldsymbol{\varepsilon}}^t\right\}, \\ \sum_{t=2}^{N_t} \left[\mathcal{M}^{*t}\right] \left[S^t\right] \left\{\underline{\boldsymbol{\sigma}}^*\right\} &= \sum_{t=2}^{N_t} \left[\mathcal{M}^{*t}\right] \left\{\underline{\hat{\boldsymbol{\sigma}}}^t\right\}, \\ \sum_{t=1}^{N_{t-1}} \left[\mathcal{M}^{**t}\right] \left[S^{t+1}\right] \left\{\underline{\boldsymbol{\varepsilon}}^{**}\right\} &= \sum_{t=1}^{N_{t-1}} \left[\mathcal{M}^{**t}\right] \left\{\underline{\boldsymbol{\varepsilon}}^t\right\}, \\ \sum_{t=1}^{N_{t-1}} \left[\mathcal{M}^{**t}\right] \left[S^{t+1}\right] \left\{\underline{\boldsymbol{\sigma}}^{**}\right\} &= \sum_{t=1}^{N_{t-1}} \left[\mathcal{M}^{**t}\right] \left\{\underline{\hat{\boldsymbol{\sigma}}}^t\right\}, \end{cases} \quad (15)$$

with,

$$\begin{aligned}\left[\mathcal{M}^{*t}\right] &= \left[S^t\right]^{\mathrm{T}}\left[p^t\right],\\ \left[\mathcal{M}^{**t}\right] &= \left[S^{t+1}\right]^{\mathrm{T}}\left[p^t\right].\end{aligned} \tag{16}$$

Stationary with respect to $\left[S^t\right]$, to update the state mapping, is difficult to explicit. Indeed, contrary to other variables, which are continuous numbers of $\mathbb{R}$, $[S]$ is made of discrete numbers of $\mathbb{N}$. As a consequence a brute force method is employed. Detailes are given in Section000000000000000000000000000 2.4.

The resolution of such a problem has already been discussed in [23, 35]. It relies on a staggered algorithm that computes alternatively the Lagrangian multipliers and the correction of the stress fields for a given material state set and selection matrices (called the mechanical problem), then the update of the material states set and selection matrices for given stresses (called the material problem). These two steps are discussed in the next sections.

2.3 | Resolution of the mechanical problem

Let us consider a given set of material states $\left(\left\{\underline{\boldsymbol{\varepsilon}}^*\right\},\left\{\underline{\boldsymbol{\varepsilon}}^{**}\right\},\left\{\underline{\boldsymbol{\sigma}}^*\right\},\left\{\underline{\boldsymbol{\sigma}}^{**}\right\}\right)$ and a given mapping through the selection matrix $[S]$.

They can be initialized using experimental strains, a first guess for the stress fields and basic K-means algorithm. In the present case, an FE simulation with imposed experimental loads is first performed using an arbitrary elasto-plastic model. An elastic initialization could also be used but would necessarily increase the number of iterations and potentially converge to local minima. Initializing the problem with a model also provide a route for improving it since it eventually allows for emphasizing areas, in the constitutive space, where *DDI* deviates from the model giving clues for its improvement.

The mechanical problem can be solved by substitution, leading first to the computation of the Lagrangian multipliers:

$$\underbrace{\left[\hat{\underline{\boldsymbol{B}}}\right]^{\mathrm{T}}[w]^{\mathrm{T}}\left[p^t\right]^{-1}[w]\left[\hat{\underline{\boldsymbol{B}}}\right]}_{[\mathcal{M}^t]}\left\{\lambda^t\right\} = \underbrace{\left[\hat{\underline{\boldsymbol{B}}}\right]^{\mathrm{T}}[w]^{\mathrm{T}}\left\{D^t\right\} - \alpha^t\left\{\hat{f}^t\right\}}_{\{b^t\}} \quad \forall t \in [1, N_t]. \tag{17}$$

It consists in a set of N_t systems of $\hat{N}$ independent linear equations to solve. This is done using a Cholesky decomposition:

Finally, stresses are updated using the second line of the system of equations 13.

$$\left\{\hat{\underline{\boldsymbol{\sigma}}}^t\right\} = \frac{1}{\alpha^t}\left(\left\{D^t\right\} - \left[p^t\right]^{-1}[w]\left[\hat{\underline{\boldsymbol{B}}}\right]\left\{\lambda^t\right\}\right), \forall t \in [1, N_t]. \tag{18}$$

2.4 | Resolution of the material problem

First, the mapping operator, *i.e.* $[S]$, must be computed for given stress fields and the actual set of material states. As mentioned above this is done in a brute force way, finding for each element e the material state N_i^* that is the closest with respect to $\|\|^2_{\mathbb{C}_o}$. This is relatively expensive as it requires, for each mechanical state, to compute its distance to all material states in the material database. This operation is the bottleneck of the method.

Once this matrix obtained, the set of material states $\left(\left\{\underline{\boldsymbol{\varepsilon}}^*\right\},\left\{\underline{\boldsymbol{\varepsilon}}^{**}\right\},\left\{\underline{\boldsymbol{\sigma}}^*\right\},\left\{\underline{\boldsymbol{\sigma}}^{**}\right\}\right)$ is actualized using Eq. 15. The complexity of the resolution mainly depends on the form of $\left[p^t\right]$. If $\left[p^t\right]$ is diagonal, as it has always been the case in the literature according the author knowledge, the resolution of Eq. 15 simply consists in computing $5 \times 3N^*$ independent averages or weighted averages of the mechanical states in elements assigned to each material states through $[S]$. For example current and former material strains are found such as:

$$\begin{aligned}\underline{\boldsymbol{\varepsilon}}_i^* &= \frac{\sum_{t=2}^{N_t}\sum_{j=1}^{3N_e}\left(S_j^i\right)^t\left(p_j^k\right)^t\underline{\boldsymbol{\varepsilon}}_k^t}{\sum_{t=2}^{N_t}\sum_{k=1}^{3N_e}\sum_{j=1}^{3N_e}\left(S_j^i\right)^t\left(p_j^k\right)^t\left(S_k^l\right)^t},\\ \underline{\boldsymbol{\varepsilon}}_i^{**} &= \frac{\sum_{t=1}^{N_t-1}\sum_{j=1}^{3N_e}\left(S_j^i\right)^{t+1}\left(p_j^k\right)^t\underline{\boldsymbol{\varepsilon}}_k^t}{\sum_{t=1}^{N_t-1}\sum_{k=1}^{3N_e}\sum_{j=1}^{3N_e}\left(S_j^i\right)^{t+1}\left(p_j^k\right)^t\left(S_k^l\right)^{t+1}}\\ &\qquad \forall i \in [1:3N^*]\end{aligned} \tag{19}$$

The next section discusses the choice of such diagonal $\left[p^t\right]$.

2.5 | Choice of a Weighing matrix

The weighing matrix of the elementary distance between one mechanical state to its corresponding material state $[p]$, introduced in the *DDI* norm (see Eq. 8), can be wisely used as a natural filter for noisy experimental inputs. Input of the *DDI* being itself an output of the DIC inverse problem, it is necessarily biased and corrupted by noise. Finding a way to mitigate this issue is crucial for the application of the *DDI* method in real life experiments. Some solutions have already been proposed in the literature for such a weighting matrix.

Evenif it has not been explicitly written as such in literature, two cases can be found: (1) $\left[p^t\right] = \mathbf{I}_2$, the identity matrix [], and

(2) $\left[p^t\right] = [w]$. The first solution gives an equal weight to every elements, strain components and time-steps. The authors found it useful when the objective is to identify stresses in vicinity of a localization band using a refined mesh hence where the sought information is localized in space and time. Indeed, the second option, classical for FE integrals, gives more weight to large and undistorted elements discarding data arising from spatial localization.

2.6 | Schematic of the global minimization problem

To summarize, the resolution of the global minimization problem, *i.e.* computing $\left(\left\{\underline{\boldsymbol{\varepsilon}}^*\right\}, \left\{\underline{\boldsymbol{\varepsilon}}^{**}\right\}, \left\{\underline{\boldsymbol{\sigma}}^*\right\}, \left\{\underline{\boldsymbol{\sigma}}^{**}\right\}\right)$, $\left[\underline{\hat{\boldsymbol{\sigma}}}\right]$ and $[S]$, is performed using the following staggered algorithm [18]:

1. initialize $[\hat{\boldsymbol{\sigma}}]$ using a FE simulation with a arbitrary model
2. normalize input dataset to get $\left(\left[\underline{\hat{\boldsymbol{\sigma}}}\right], \left[\underline{\boldsymbol{\varepsilon}}\right]\right)$
3. initialize $\left(\left\{\underline{\boldsymbol{\varepsilon}}^*\right\}, \left\{\underline{\boldsymbol{\varepsilon}}^{**}\right\}, \left\{\underline{\boldsymbol{\sigma}}^*\right\}, \left\{\underline{\boldsymbol{\sigma}}^{**}\right\}\right)$ and $[S]$ using a k-means algorithm [25] on $\left(\left\{\underline{\boldsymbol{\varepsilon}}^t\right\}, \left\{\underline{\boldsymbol{\varepsilon}}^{t-1}\right\}, \left\{\underline{\hat{\boldsymbol{\sigma}}}^t\right\}, \left\{\underline{\hat{\boldsymbol{\sigma}}}^{t-1}\right\}\right) \forall t \in [1, N_t]$,
4. solve the mechanical problem (see Sec. 2.3),
5. solve the material problem (see Sec. 2.4),
6. iterate step 5 until convergence of $[S]$. It usually takes less than 3 iterations to converge
7. iterate steps 4 through 5 until convergence of $[S]$ and $\left[\underline{\hat{\boldsymbol{\sigma}}}\right]$. One iteration from step 4 to 5 will be called a cycle.

2.7 | Parameters of the method

Once the framework of the *DDI* method fixed, meaning that a particular constitutive space (see Eq. 5) and a particular norm (see Eq. 8) are selected, 5 parameters remain to be adjusted by the user and will affect performances of the algorithm.

- the number of material states N^* sampling the material response
- the amplitude and the exact form of $\mathbb{C}_o$ within the norm
- the two convergence criteria
- and the Weighing matrix of mechanical states $[p]$

The first one and part of the second one has already been investigated by Dalémat and her co-authors in [4]. They compared the stresses of FE simulations, considered as the reference, to the one obtained using the *DDI* with different number of material states values. They concluded that a small number of material states leads to an insufficient sampling of the strain-stress manifolds, and thus, to significant error. A high number of material states also leads to significant error, since it will give more weight to outliers and increase the sensitivity to noise (similarly to the overfitting phenomenon for regressions). In their work, the authors recommend a number of material states so that $20 \leq \frac{(N_t-1)\cdot N_e}{N^*} \leq 100$. The influence of the magnitude of $\mathbb{C}_o$ was found to be straightforward. Indeed, Eq. 7 shows that by choosing a tensor with high values, the normalization will give more weight to strains compared to stresses. So it may be relevant to use high amplitude to give more weight to strains which are obtained experimentally, compared to stresses which are unknowns and change during the method.

While the influence of the magnitude of $\mathbb{C}_o$ is straightforward, the influence of the symmetry class of the tensor remains unknown. In the present work, the fourth-order tensor that will be used is a Hooke tensor for an isotropic material, hence its definition will only be dependent of the choice of a pseudo-Young modulus E_o (the magnitude) and a pseudo-Poisson ratio ν_o. Nevertheless, it seems reasonable to assume that the use of a pseudo isotropic elastic tensor would not necessarily lead to a satisfying clustering, for instance, of anisotropic mechanical states. However, to the author knowledge, the question of the influence of the symmetry class of $\mathbb{C}_o$ has not yet be investigated and it is not the objective of the present work.

Regarding the two convergence criteria needed for resolution, this work proposes the following expressions:

- for the material problem criterion, we use the convergence rate of the data-driven distance Ψ (see Eq. 9) at each each iteration i. That is to say:

$$\frac{|\Psi_i - \Psi_{i-1}|}{\Psi_0} \geq \epsilon_{mat} \tag{20}$$

  where Ψ_0 is its initial value and ϵ_{mat} the user criterion

- for the mechanical problem criterion, we use the convergence rate of the norm of internal forces (See Eq. 4). That is to say:

$$\begin{gathered}\frac{|\mathcal{F}_i - \mathcal{F}_{i-1}|^2}{|\mathcal{F}_0|^2} \geq \epsilon_{mech} \\ \text{with, } \mathcal{F} = \sum_{t=1}^{N_t} \left[\underline{\hat{\boldsymbol{B}}}\right]^{\mathrm{T}} [w]^{\mathrm{T}} \left\{\underline{\hat{\boldsymbol{\sigma}}}^t\right\}\end{gathered} \tag{21}$$

Regarding the Weighing matrix two options will be compared in this paper.

$\mathcal{H}_0$: $\left[p^t\right] = \mathbf{I}_2, \forall t \in [1, N_t]$,

$\mathcal{H}_1$: $\left[p^t\right] = [w]$

Inputs	Outputs	Parameters	Assumptions
$\left[u_{\text{dic}}\right], \{F\}$	$[S]$	$\mathbb{C}_o$	Plane stress
$[B]$	$[\hat{\sigma}]$	N^*	Small strain
$\left[\sigma_{\text{fe}}\right]$	$\{\varepsilon^*\}, \{\varepsilon^{**}\}$	$\epsilon_{mat}, \epsilon_{mech}$	Constitutive space
	$\{\sigma^*\}, \{\sigma^{**}\}$	$[p]$	
	Ψ		

TABLE 1 Summary of the inputs, outputs, parameters and the assumptions needed for the Data-Driven Identification method proposed in this work. In this table, Ψ gives the *DDI* distance at convergence.

Table 1 summarizes the inputs, outputs, parameters and assumptions needed for the proposed Data-Driven Identification method. It emphasis the fact that, evenif *DDI* presents itself as a model-free technique for fields of stress tensors identification, part of the modelling framework is hidden in the choice of the constitutive space. Nevertheless, while the framework is constrained the exact form of the constitutive equation remains free. Moreover, the role of user parameters remains significant and many aspects has still to be investigated. The three main output of the method are useful in different ways: (1) the value of the converged *DDI* distance Ψ gives information about local and global quality of the stress solution. Indeed, if the scattering remains high the distance will be high emphasizing either issues with input noise, user parameters or dimensionality of the constitutive space. A proper analysis of this distance may help to improve the constitutive space. Indeed, if relevant dimensions are not taken into account, *e.g.* temperature in a test where an external heat source imposes very high thermal gradients, it will lead to a significant scattering of the data within the chosen sub-space. (2) Mechanical points allows for probing locally (time and space) the mechanical response, for instance in vicinity of crack tip, allowing to access mechanical response in never-seen loading conditions but remain as for DIC, potentially noisy. (3) Material states average the mechanical response and sample, within the constitutive space, an underlying constitutive equation. This quantity could eventually be used to identify a parametric form of a constitutive equations.

3 | EXPERIMENTAL METHOD

The *DDI* method has been presented and detailed previously. In this section, the experiment investigated will be presented. It consists in a high-speed tensile test performed on a metal sheet with a specific geometry.

3.1 | Specimen material

The material chosen for this experimental campaign is the rate-dependent, low-carbon mild-steel XES (French standards). Its chemical composition is presented in Tab. 2. The quasi-static and dynamic behaviour of this material are relatively well-known. Indeed, for example in the mid 90s, methodologies were developed allowing to perform double-shear experiments on thin metal sheet in both quasi-static and high strain-rate conditions with highly homogeneous stress and strain states [11]. These methodologies were used to study the shear behaviour of the XES steel – in particular the evolution of the rate sensitivity, for strain-rates ranging from $1\times10^{-3}\,\text{s}^{-1}$ to $1\times10^{3}\,\text{s}^{-1}$ [17]. The tensile behaviour of this steel has also been investigated. For this purpose, Haugou and its collaborators [12] developed a tensile testing device for split Hopkinson bars. This device allows for non-direct tensile tests to be performed on metal sheets. The configuration was used to characterize the mild-steel for plastic strain-rates between $180\,\text{s}^{-1}$ and $440\,\text{s}^{-1}$. At last, more recently, some researchers focused on the modelling of spot weld for this material. For instance, using experiments based on Arcan principle, Langrand *et al.* [19, 20] were able to model and characterize the joint when submitted to pure and mixed tensile/shear loads in both quasi-static and dynamic conditions. In 2016, Markiewicz *et al.* [26] went one step further and investigated the behaviour of the material when heat affected by spot welding. Furthermore, the authors studied the strain-rate dependency of the heat affected material and identified parameters (see Tab. 3) for modified Krupkowsky model [30], which is a visco-plastic model (rate-dependent hardening flow model) describing the material. This model is written as:

$$\begin{aligned} \sigma_{KR} &= KX^a\left(\varepsilon_0 X^b + \varepsilon_p\right)^{nX^c}, \\ \text{with } X &= \frac{\dot{\varepsilon}_p}{\dot{\varepsilon}_0}, \end{aligned} \tag{22}$$

where K, a, b, c, n, ε_0 and $\dot{\varepsilon}_0$ are the model parameters to be identified. It is inspired from the the Krupkowski hardening flow model (also named Swift hardening model) [], widely used in FEM software, itself inspired from the Hollomon (or Ludwig) hardening flow model [], both used to model quasi-static mechanical responses in plastic regime. Notice that, at the limit of zero strain-rate, modified Krupkowsky model tends to its peer. It translates the complex relationship between plastic yield, hardening and strain-rate that a more simple model, *e.g.* Johnson-Cook, can not capture. Fig. 2 shows the mechanical response of XES for various strain-rates with the fitted model.

C	S	N	Mn	P	Si	Al	Ni	Cr
0.0268	0.0175	0.006	0.202	0.007	0.007	0.07	0.018	0.036
Cu	Mo	Sn	Nb	V	Ti	B	Ca	
0.014	0.002	0.004	0.001	0.002	0.002	≤ 0.0003	≤ 0.0003	

TABLE 2 XES chemical composition (in wt%), data from [26].

Parameters	K (MPa)	ϵ_0	n	$\dot{\epsilon}_0$ (s^{-1})	a	b	c
[26]	526.6	0.024	0.221	0.085	0.0002	0.385	0.002

TABLE 3 Parameters for the modified Krupkowsky model from [26].

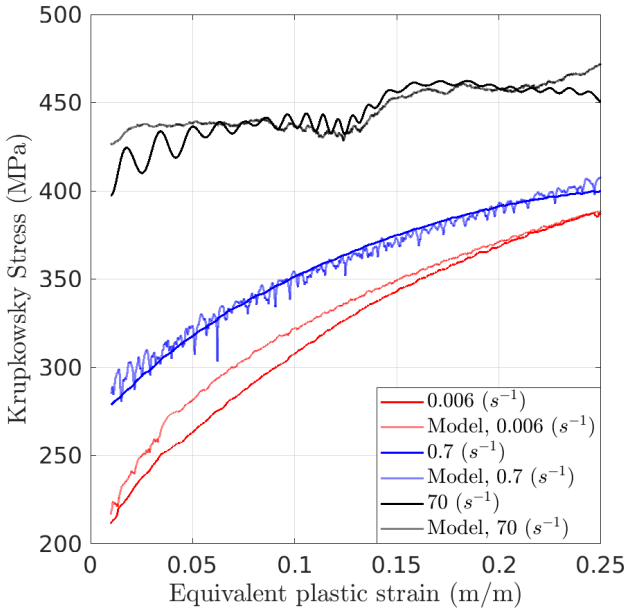

FIGURE 2 Reference data and modified Krupkowsky model previsions from [26].

3.2 | Specimen geometry

The chosen specimen geometry is derived from the one classically used when using a hydraulic tensile test machine (see the next section for more details). Indeed, the use of such a device limits the specimen length and width. In addition, since the *DDI* method relies on the load recorded by the load cell, the sample needs to be symmetrical in the tensile test direction in order to avoid the introduction of any bias in the load measurement (*e.g.* transverse loading).

The main features of the geometry are two symmetrical notches and a central hole (see Fig. 3). Such features are expected to lead to strain concentration bands between the notches and the central hole as well as secondary bands from the central hole to the edge of the sample with an angle of approximately 45°. Hence, the use of such a geometry during one high speed tensile test allows to capture the material's response for wider ranges of strains and strain-rates compared to the standard geometry as well as creates heterogeneous stress-strain states within the specimen. The specimens were were cut from a 0.8 mm-thick metal sheet in the rolling direction.

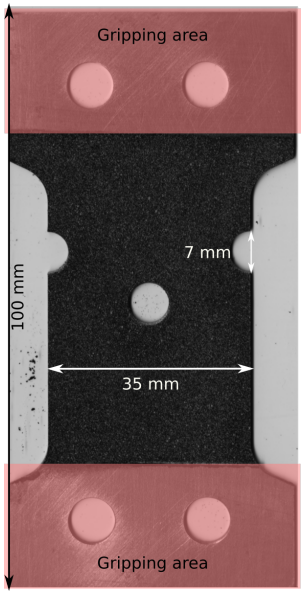

FIGURE 3 Photography of an experimental sample, its principal features are two symmetrical notches and a central hole.

3.3 | Experimental setup

The tests conducted in this work are high speed tensile tests. They are conducted using a hydraulic tensile test machine (MTS-819, 20 kN). On this machine, the upper grip is mounted on a modified Hopkinson bar, similarly to the device from [21]. This bar is made of steel (42CD4 rectified) and is instrumented

with strain gauges in order to act like a load cell (see Figure 4). In addition, the lower grip is mounted on a sliding bar. The sliding bar is in an enclosing case linked to the actuator. The sliding bar, through the control of the "free fall" length, allows the actuator to reach the imposed displacement speed before loading the sample. The maximum actuator velocity allowing an accurate load measurement, *i.e.* 5 m s^{-1}, is used for this experiment. The "free fall" distance was accordingly set to 25 mm.

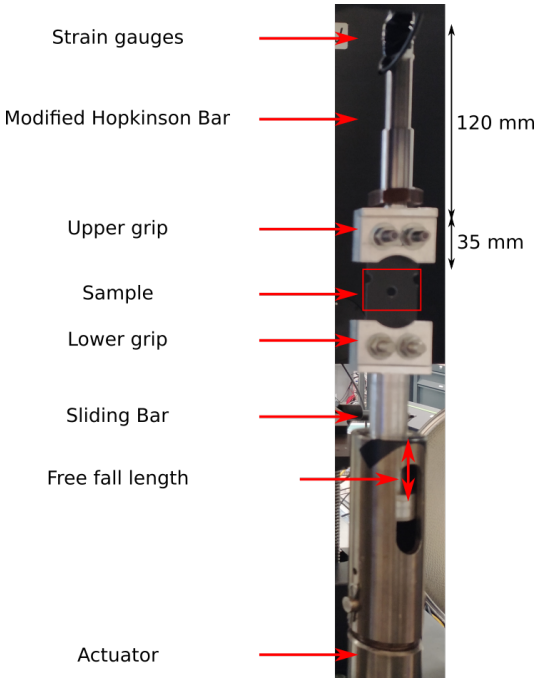

FIGURE 4 Close-up view of the high speed tensile machine setup.

3.4 | Imaging setup

The camera used in this work is a Cordin-580. It is a rotating mirror camera that captures 78 images of 8 megapixels (2472 x 3296 pixels) up to 4 million fps. This camera and its specificities have been studied in depth in [36]. For the experiment presented in this work, the camera is equipped with a 90 mm Tamron objective, and records at 68 kfps with a CDS gain of -3 dB (Correlated double sampling) and a CCD gain of 15 % (amplification factor in the analog-to-digital converter). At such speed, the film duration is about 1.18 ms. In order to provide enough light, two Pro-10 (2400 J each at 10-stops) Xenon flashes from Profoto are used. They are set in normal mode, at 10 f-stops. In that configuration, the illumination typically lasts 2.4 ms with a stable and optimal plateau of 1.1 ms. The flashes and the camera are triggered separately in this experiment. The flashes are triggered using an infrared light-gate system (SPX1189 series Honeywell). It is placed in such manner that it is obscured by the enclosing case. The optical gate will then send a 5 V TTL signal when the enclosing case is at a given distance to the contact with the sliding bar. This distance has to take into account the speed of the actuator as well as the rising time of the flashes (150 µs). It has been empirically determined and set at 3.7 mm from the contact point. The Cordin-580 is triggered using the load cell. When the load reaches a chosen threshold (in this study 6231.5 N, ≈ half of the plastic yield), a trigger is sent to the camera. Upon receiving the trigger, the camera will record the following images, as well as the ones taken up to 100 µs before (this is named post-triggering). These parameters were determined empirically through preliminary tests. Furthermore, the working distance between this camera and the sample is about 31 cm, leading to a pixel size of 14.49 µm. These information are summarized in Tab. 4.

An infrared camera (a Telops M3K) is also used to record the other face of the sample during the experiment (see Fig. 5). The infrared results fall out of the scope of the presented work. Nevertheless, thermal information confirmed that no strong thermomechanical couplings are induced by the strain. Indeed, mean sample temperature rises up to 5 °C while the temperature within localization band does not exceed 50 °C before fracture onset. It confirms that the constitutive space used to identify stresses does not have to take into account explicitly temperature (see Sec. 2).

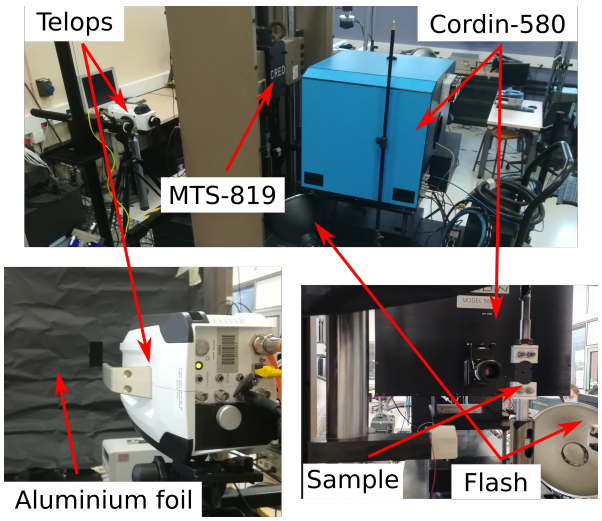

FIGURE 5 Experimental setup for a high speed tensile test, recorded using a visible-light camera and an infrared one.

Camera	Cordin-580
Image resolution	2472 pixels × 3296 pixels
Dynamic Range, Detector	12 bits
Dynamic Range, Image	16 bits
Acquisition Rate	68 kfps
Lens	Tamron SP 90 mm Di Macro
Aperture	f/2.8
Field of view	35.8 mm × 47.8 mm
Image scale	1 pixel = 14.49 µm
Stand-off distance	31 cm
Patterning Technique	Black and White paint

TABLE 4 DIC hardware parameters.

DIC Software	Ufreckles [31]
Shape Function	linear FE triangle elements
Matching Criterion	element-wise ZNSSD
Image Filtering	sensor flattening (vignetting)
Data Processing	U : Tikhonov regularization over 4 elements
Data Post-Processing	$\dot{\epsilon}$: Savitzky–Golay filter of order 2 applied onto U (win = 23 fr)

TABLE 5 DIC analysis parameters.

3.5 | DIC setup and parameters

In order to be able to perform DIC on the images recorded by the camera a reference image is needed [36]. In this work, this image is obtained by recording the black and white paint speckle pattern on the sample using a high definition camera (50M pix, Prosilica GT from Stemmer) combined with the same objective lens as the one used with the Cordin-580, prior to the test. Furthermore, following this methodology, 12 calibration shots were taken with the Cordin camera when the first sample was mounted, prior to the test. These calibration shots are used in order to create a representative model of the distortions induced by the camera in experimental conditions (lens, working distance, magnification, frame rate). Then, in order to correct the eventual rigid body motion between one experiment and the other, a single calibration shot is performed before each of the other experiments.

In this work, a continuous mesh is used. Since it is known that strain localization appears in 2 principal bands, the mesh is refined along these bands and in the vicinity of the notches and the hole as well. The element size is 32 pixels on average, but finer along the crack (about 26 pix). A Tikhonov regularization of the DIC problem of 4 elements is used to filter-out spatial noise. The displacements are firstly pointwise convolved with a rolling temporal Savitzky-Golay filtering window of second order with a window size equal to 23 frames (see Tab. 5). Then strain-rates are obtained from strains using a simple 1^{st} order finite difference scheme. Such data filtering marginally affects strain, but significantly decreases the amount of noise on strain-rates.

3.6 | Technical issues and solutions

Due to the complexity of the experiments conducted, some technical issues have to be tackled. This is the aim of this section.

Load measurement

The load is captured by the load cell during the experiment. However, it has to be adjusted time-wise: indeed, the load is measured by strain gauges while the information is needed on the mesh boundary, in particular for the *DDI* (see Sec. 2). Hence, due to the distance between the mesh boundary and the strain gauges, a delay has to be taken into account. Figure 4 presents the experimental apparatus, with in particular the distances of interest: the distance between the strain gage and the grip (120 mm using the constructor's data) as well as the distance between the grip and the ROI ($\approx$ 35 mm measured manually). Then, using the modified bar's properties (E = 205 GPa and $\rho = 7850\,\mathrm{kg/m^3}$), the delay is computed as follows: $\tau = \frac{\sqrt{\rho}}{\sqrt{E}}$, which yields a delay of 30 µs. This is in the order of magnitude of two Cordin interframes for this experiment. Furthermore, note that even an error of 1 cm in the distance between the grip and the ROI leads to an error of 2 µs for τ, which is negligible regarding our time resolutions.

Pre-stressed sample

The experimental setup is hyper-static, and as a result, the sample when fixed is already pre-constrained. Indeed, the griping device relies on two metallic rods on each side of the sample to maintain it. However, due to its use, the rods are deformed. As a result the sample may be already slightly deformed when placed, before the experiment. This can be evidenced by looking at the displacement fields obtained for the shot taken when the sample is in place and static. A rigid-body motion identified on the first image is subtracted to these fields in order to account for a possible small rotation between the reference image (taken with another camera in a different set-up) and the Cordin images. Figure 6 depicts the averaged over time of the axial and transverse displacement fields with the rigid-body motion subtracted as well as the averaged over time Von-Mises norm of the total strain. This figure shows that the sample is under vertical tension on the right-hand side, as well as horizontal tension on the bottom. Nevertheless, the amplitude of these tensions are about $\pm$ 1 pixels. Furthermore, the averaged over time Von-Mises norm

of the total strain clearly shows that the sample is slightly deformed (less than $3\,\mathrm{mm\,m^{-1}}$), which is in the same order of magnitude as the strain measurement uncertainty. Hence, the sample may be pre-constrained by the experimental setup, nevertheless this phenomenon is not significant.

4 | NUMERICAL TWIN

In order to investigate the Data-Driven Identification method introduced in Section 2 and the influence of the user parameters, especially the weighing matrix $[p]$, a numerical validation is conducted and is presented in this Section. Note that, contrary to classical 1D loading cases, the presented work relies on data existing in a 13 dimension space (3 for $\boldsymbol{\varepsilon}$, 3 for $\dot{\boldsymbol{\varepsilon}}$, 3 for $\boldsymbol{\sigma}$, 3 for $\dot{\boldsymbol{\sigma}}$). Such high dimensionality requires developing new ways to display results. Nevertheless, such developments go beyond the scope of this work. Hence, for the sake of simplicity the majority of the results will be presented in sub-spaces using invariant based norms (*e.g.* I_1, Von-Mises). Note that this is not a requirement but just a graphic choice. Any other mechanical norms could have been chosen.

4.1 | Creation of a Numerical twin

The Virtual Image Deformation (VID) is a process that consists in making a numerical twin of an experiment. The use of such a numerical twin allows to have access to a realistic estimation of the data that will be measured during the real experiment. Furthermore, it allows to qualify an experiment in terms of measurability of the fields of interest (in the present case the stress tensors), and their uncertainties. It can also validate an identification procedure and its robustness with respect to realistic experimental conditions. In order for this procedure to be relevant, VID must take into account, as much as possible and as accurately as possible, experimental errors and uncertainties such as:

- The spatial resolution of the imaging system and the DIC sampling, which affects the ability to capture strain gradients,
- The temporal resolution of the imaging system, which affects the temporal derivatives (speed, acceleration),
- In our particular case, when using the Cordin, the bias induced by the camera's distortions which lead to low but still non-negligible displacement uncertainties,
- Sensor noise, which affects the optical flow conservation in DIC and thus displacement uncertainties as well as time derivatives.

Obviously such procedure is never perfect, for instance, it is difficult to take into account strong speckle transformation or even degradation in highly deformed regions during large strains [37], light variation, out-of-plane motions... For these reasons, the use of VID is becoming more and more systematic in the validation of an experimental procedure and of inverse identification procedure [33, 1, 32, 13, 2, 34, 8, 27, 7].

Thus, in the following paragraphs, this construction is described. Several Finite-Elements simulations will be performed using Abaqus with the implicit solver using CPS3T elements. In all the FE simulations the thermomechanical Johnson-Cook model will be used as it is implemented by default in FE solvers. Particular attention is given to the influence of the initial solution used in *DDI*, especially since the Johnson-Cook model is not able to fully capture the complex strain-rate dependency of the material that will be investigated.

Creation of a reference solution (U^{ref}, $\boldsymbol{\sigma}^{\mathrm{ref}}$, F_y^{ref})

A FE simulation is first performed in order to create a reference solution, which will serve 2 purposes : (1) the construction of Virtual images, (2) to compare the results after using the whole chain leading to the estimation of stress tensors (DIC + *DDI*). This simulation is conducted using the model parameters given in in Tab. 7 (this will be called Model A in the rest of this work). They are identified using a tensile test at an average strain-rate of $70\,\mathrm{s^{-1}}$ from a previous study [26]. To mimic the experiments, the simulation is performed under imposed displacements on the upper and lower boundaries. On the upper boundary a 0 displacement fields is imposed in both the axial and transverse directions as it is gripped. On the lower boundary, a displacement corresponding to a velocity of $5\,\mathrm{m\,s^{-1}}$ is imposed in the axial direction. For simplicity purposes, this simulation is performed using an experimental DIC mesh that was used for the actual experiment. The same mesh will be used throughout the whole procedure.

The outputs of this simulation – namely the displacement fields $\boldsymbol{U}^{\mathrm{ref}}$, the stress fields $\boldsymbol{\sigma}^{\mathrm{ref}}$ and the vertical net force on the upper boundary F_y^{ref} – will be used as references for what follows.

Virtual image deformation

In order to be able to perform DIC on the synthetic images, a texture needs to be applied. For this study a classical black and white paints speckle pattern is considered. The undistorted reference image is thus created using a high resolution camera to record a speckle pattern made with black and white paints. This reference image is then binned down to the Cordin image size. Then, using the same mesh as FE simulation, this image is cropped resulting in the image in Figure 7a. The field of view (cm x cm, see Table 6) matches the aspect ratio of the camera for a pixel size of µm (*i.e.* a magnification of).

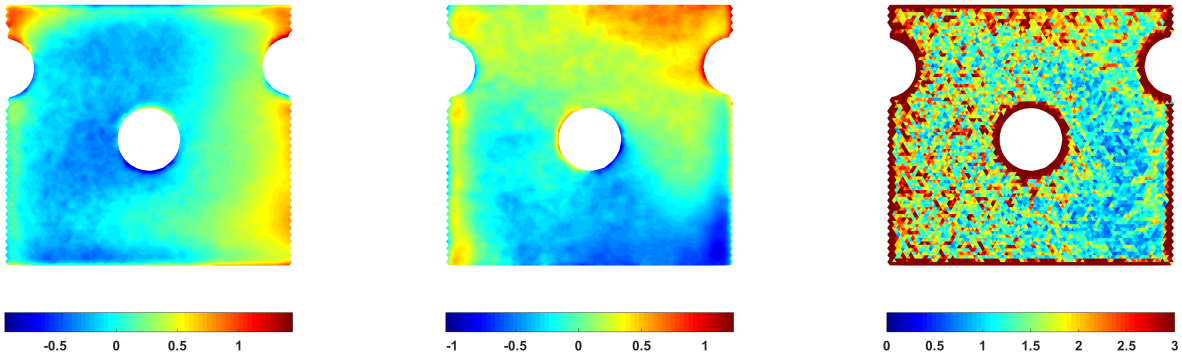

(a) Time average U_x (pix), **(b)** Time average U_y (pix), **(c)** Time average $||\varepsilon_t||_{VM}$ (mm/m),

FIGURE 6 Averaged over time displacement fields and Von-Mises norm of the total strain when the sample is placed in the gripping device and static (1 pixel = 14.5 µm).

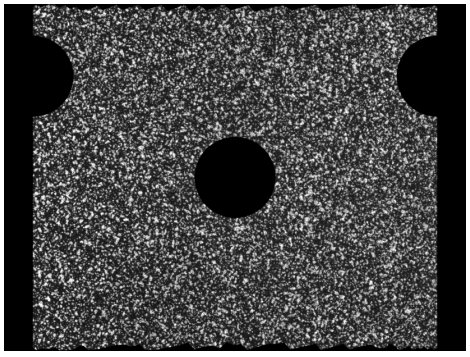

(a) Reference image created synthetically,

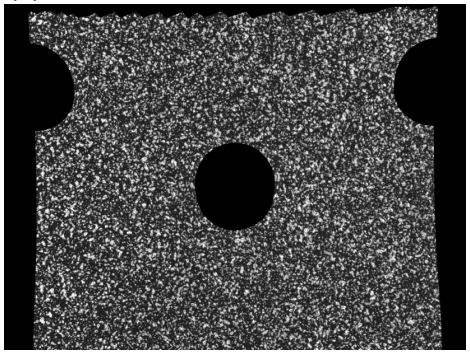

(b) Deformed and distorted image,

FIGURE 7 Example of the reference image and a deformed and distorted image created synthetically.

Once the reference image created, using the mesh and the displacement fields from the reference simulation, the image is deformed (see Fig. 7b for an example). This is done by performing a loop on the elements of the deformed mesh. For each element, the pixels contained in it are known. Using shape functions and inverse mapping, their position in the undeformed picture is obtained. Their associated grey values can then be retrieved by performing a spatial bi-cubic spline interpolation of the grey value of the reference image. This process is summarized in Figure 8.

FIGURE 8 Schematic of the deformation procedure of a synthetic image for one triangular element. The black squares depict the pixels positions in the deformed configuration, while the grey squares depict the pixels positions in the reference one. The red crosses denote the pixels from the deformed configuration projected by an inverse mapping in the reference one. The deformed image for the element is obtained by interpolating the grey levels from the grey squares onto the crosses.

Furthermore, in order to be as representative of a real experiment as possible, measurement bias introduced by the distortion variability from one shot to another has to be taken into account. For simplicity purpose, two sets of distortion parameters obtained experimentally are used. The first one (obtained for a specific calibration shot) is used to deform the images and the second one (which is from the statistical distortion model associated to the first set of parameters) is used to perform DIC.

As a result, this allows to introduce the right order of magnitude of uncertainty in displacement measurement inherent to the method. Using the composition relationship between the effective displacement u_{simu} and the first distortion field u_d, the imposed displacement u_{virtual} used to deform the images is computed as follows:

$$u_{\text{virtual}}(\underline{X}) = u_{\text{simu}}(\underline{X}) + u_d(\underline{X} + u_{\text{simu}}(\underline{X})). \tag{23}$$

Finally, a realistic noise is added to the deformed and distorted synthetic images. The estimation of grey level noise, meaning apparent grey level variation of one material points from one image to another over time, has been estimated as follows:

- Images of a static reference shot of the sample are deformed back to the undistorted configuration using identified distortion parameters. At that stage, each pixel sees the same material point over time.
- The grey level standard deviation over time of every pixel is computed and its normalized value (by the pixel's grey level) plotted as a function of the mean grey level value of the considered pixel. The plot is presented in Figure 9. This database can be fit with a polynomial P to get the trend of the apparent noise of the camera over its dynamic. The polynomial used is depicted in the figure by the black line.
- This result is used to add random noise to images proportional to pixel grey levels following this equation:

$$\text{noise}(F, p) = F(p) \cdot P(F(p)) \cdot \text{randn}(p), \tag{24}$$

where $\text{noise}(F, p)$ is the noise that will be added to the pixel p of image F, $P(F(p))$ is the noise value fit by the polynomial for the grey value $F(p)$ and randn is a normally distributed random numbers matrix of the size of F.

At the first order, the polynomial fit shows that the apparent noise converges toward 5 % in the whites, reaches 10 % at about 12 bits (4000) then ramps up to 30 % in the blacks. Notice that, in practice, data presented in Figure 9 is not strictly speaking a noise. Indeed, pixel time variations are in our case not only due to CCD dark noise but to the offset and gain mismatch from one sensor to another, the focus mismatch, as well as the uncertainty on distortion estimation which does not allow for perfectly stabilizing images (± 0.1 pixel). This is why we name it apparent noise. In addition, it explains why values are very high compared to mono-sensor ultra-high speed camera (*e.g.* in the order of 1 % of 16 bits for the Shimadzu HPV-X). Nevertheless, apparent noise will affects the optical flow conservation in a similar way to real noise and will have a strong impact on time derivatives.

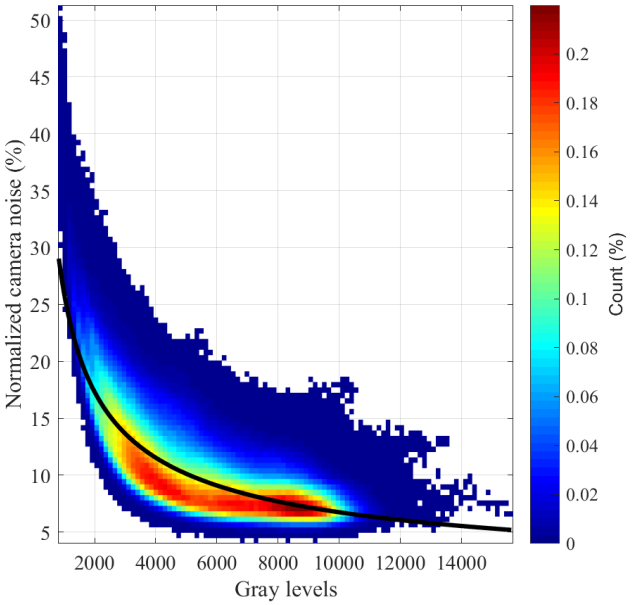

FIGURE 9 Normalized apparent camera noise (in %) versus the mean grey level. The colour denotes the counts (in %), while the black line denotes the polynomials used to model the camera noise.

As a summary, at this stage we have to produced, references kinematic fields as well as images that mimic the response of our imaging system. Applying the dedicated DIC procedure for the Cordin camera allows for capturing realistic displacement fields U^{DIC}. In the next section, the *DDI* method will be investigated using these fields in order to assess its accuracy as well as the influence of user parameters.

DIC Software	Ufreckles [31]
Image size	2472 x 3296 pixels
Field of view	cm x cm
Cordin pixel size	5.5 µm
Image scale	1 pixel = µm (Magnification of)
Mesh size	≈ 21 pixels
Data Processing	U: Tikhonov regularization over 4 elements

TABLE 6 Virtual DIC parameters.

4.2 | Creation of a statically admissible initial solution using a "wrong" model

The creation of an initial guess for the stress field that will be used as an input for the *DDI* algorithm requires two

consecutive Finite-Element simulations. To validate the *DDI* procedure, an initialization reasonably far from the solution is chosen. To this effect, the same model as the reference one is chosen but the constitutive parameters are significantly modified. Hence, the initial yield is decreased, whereas the hardening modulus is increased. In addition, to investigate the ability of the *DDI* to accurately retrieve the strain-rate dependency, the strain-rate dependency is set close to zero. The exact parameters are given in Tab. 7 (it will be called Model B).

- The first simulation is conducted under imposed displacements, using U^{DIC}. The load profile on the upper boundary is extracted from this simulation. This profile is then rescaled in such a manner that, in the end, the net force on the upper boundary is equal to the reference net force F_y^{ref}. The role of this first simulation is to get a nice estimation of the load distribution at the upper bound of the sample.

- The second simulation is then performed under mixed boundary conditions: imposed displacements on the lower boundary, imposed displacements in the X direction and imposed rescaled vertical distribution of forces on the upper bound. This simulation allows to obtain statically admissible stresses $\boldsymbol{\sigma}^{\mathrm{false}}$.

The whole procedure is summarized in Figure 10. In what follows the *DDI* will be given the total strains $\boldsymbol{\varepsilon}_t^{\mathrm{DIC}}$ (computed from U^{DIC}) and $\boldsymbol{\sigma}^{\mathrm{false}}$ as inputs. This case allows to assess the influence of the measurement errors on the estimation of the stress fields. Hence, the final errors are representative of the ones performed during an experiment.

4.3 | Results and discussions

The *DDI* is used using 50 time steps using simulation results as described previously. First the influence of the different parameters (see Tab. 1) of the *DDI* will be investigated. Then, once the parameters chosen, the *DDI* results will be presented and discussed.

Influence of the parameters

To investigate the influence of the different parameters of the method, several computation were performed. The ration N^* varies from 30 to 200, the ratio $\frac{E_o}{E}$ varies from 0.1 to 10, the regularization length from 0 to 5 and finally the weighting matrices are either $\mathbf{I}_2$ or $[w]$. In order to assess which quadruplet leads to the best results, the following equivalent standard deviation ξ_{eq} is considered:

$$
\begin{aligned}
&\xi_{\mathrm{eq}}(\underline{\underline{\sigma}}_{\mathrm{DDI}}) = (\bar{V}(\underline{\underline{\sigma}}_{\mathrm{DDI}}))^{\frac{1}{2}},\\
&\bar{V}(\underline{\underline{\sigma}}_{\mathrm{DDI}})) = \frac{1}{3N_eN_t}\sum V(\underline{\underline{\sigma}}_{\mathrm{DDI}})),\\
&V(\underline{\underline{\sigma}}_{\mathrm{DDI}})) = \frac{1}{N_eN_t}\sum_{e,t}\Delta\sigma^{xx}(e,t)^2 - \left(\frac{1}{N_eN_t}\sum_{e,t}\Delta\sigma^{xx}(e,t)\right)^2\\
&\qquad + \frac{1}{N_eN_t}\sum_{e,t}\Delta\sigma^{xy}(e,t)^2 - \left(\frac{1}{N_eN_t}\sum_{e,t}\Delta\sigma^{xy}(e,t)\right)^2\\
&\qquad + \frac{1}{N_eN_t}\sum_{e,t}\Delta\sigma^{yy}(e,t)^2 - \left(\frac{1}{N_eN_t}\sum_{e,t}\Delta\sigma^{yy}(e,t)\right)^2,\\
&\Delta\sigma^{ij}(e,t) = \sigma^{ij}_{\mathrm{DDI}}(e,t) - \sigma^{ij}_{\mathrm{ref}}(e,t).
\end{aligned}
\tag{25}
$$

Thus, the error is the square root of the averaged variance of the difference between the estimated stresses and the reference ones for all the spatio-temporal elements and all the stress components. This error allows in one scalar to take into account each component of the stress tensors for all the spatio-temporal elements.

The best parameters among those tested are the following : $N^* = 30$, $E_o = 10.0 \cdot E$ where E is the steel's Young modulus, $l_c = 2$ and $[p] = [w]$. Figure 11 depicts the evolution of ξ_{eq} when 3 out of 4 parameters are fixed and one varies. This figure shows that the error increases when the number of material states decreases (*i.e.* when N^* increases). Furthermore, the error decreases when E_o increases. These trends are in line with the observations from [4]. In addition, this figure highlights that there is an optimal regularization length: $l_c = 2$. At last but not least, the choice of the weighting matrices do not have a significant influence on the error. Nevertheless, the use of $[w]$ leads to a small reduction of the error (from 24.8 % to 23.7 %).

A posteriori filtering operator

Let us consider the mechanical points distribution in the $\{||\varepsilon||_{VM}, ||\sigma||_{VM}\}$ space. This space is of interest since it is the most commonly used one for the characterization of materials. Figure 12a depicts the distribution of the mechanical points in this space. This figure shows the influence of the noise introduced in the VID procedure on the *DDI* results. Indeed, a main response is observed (characterized by mechanical states with high occurrence numbers) with a spread around it. This spread is especially important for strains beyond 40 % as it reaches more than 150 MPa. Nevertheless, the occurrences of the mechanical states in the spread are several order of magnitude below the occurrences in the main response. Since the *DDI* method is data-based, it stands for a reason that the most recurrent mechanical states are more relevant than the others. Hence, this leads to the definition of an *a posteriori* filtering to

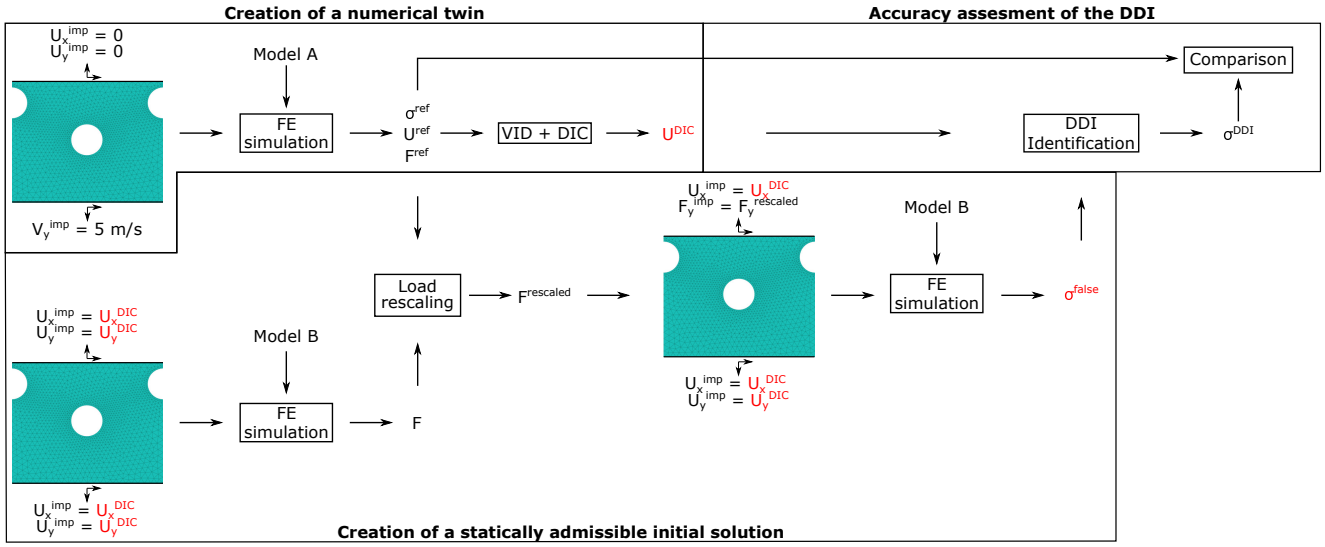

FIGURE 10 Schematic of the numerical test case procedure. In red are the inputs of the *DDI* algorithm.

	A (MPa)	B (MPa)	n	C	$\dot{\varepsilon}_0$ (s^{-1})	m	T_o (K)	T_{melt} (K)
Model A	394 MPa	136 MPa	0.471	0.0259	69.86 s^{-1}	1.11	300	1350
Model B	315 MPa	272 MPa	0.6123	2.56×10^{-4}	69.86 s^{-1}	1.11	300	1350

TABLE 7 Parameters of the two Johnson-Cook model used for the FE simulations to investigate the *DDI* algorithm.

select only theses states. In what follows, a mechanical states is considered as relevant if its occurrence is higher than the 95th quantile. Figure 12b depicts the mechanical points distribution obtained after the proposed filtering. As expected, only the main response remains and the mechanical states spread is significantly reduced. Note that when using this filtering, 9 % of the mechanical points are disregarded. This supports the use of this filter since it improves significantly the *DDI* results while disregarding a minimal amount of data. In the rest of this document, all the results will be presented after the use of the introduced filter.

Results

In order to assess the accuracy of the method and its ability to retrieve the reference stresses despite the initialization, the *DDI* stresses will be compared to the reference ones. To be as thorough as possible, the stress errors will be presented in several different spaces.

First, let us consider the stress uncertainty achieved with respect to the stress magnitude. To this effect, Figure 13 depicts the stress magnitude distribution. Furthermore, it also represents the stress uncertainty (relative in blue and absolute in red) with respect to the stress magnitude. The distribution indicates that a significant amount of data is for stress magnitudes below 200 MPa. This corresponds to the elastic behaviour of the considered material (see Fig. 12b), that is to say where the signal to ratio is not favorable due to the measurement noise on the strains. This is illustrated by the fact that the relative error is higher than 100 % for low strains and decreases until it reaches 12 % at 200 MPa. In addition, less data is available in the 200 MPa – 400 MPa range, which is also during elasticity. The impact of the data scarcity in this range can be observed with the absolute stress uncertainty. Indeed, as the data available decreases, the absolute stress uncertainty increases from 9 MPa at the beginning to 27 MPa at 315 MPa. Nevertheless, since the signal to ratio becomes favorable, the relative stress error remains below 10 % after a stress magnitude of 200 MPa. At last, more data is available beyond 400 MPa *i.e.* during plasticity. The figure shows that beyond this stress magnitude, the error remains below 16 MPa that is to say a relative error of 4 %.

Let us now investigate the accuracy of the method is the physical space. Figure 14 depicts for each element of the mesh their relative systematic and random stress errors. It can be observed that the the elements above and below the central hole and the notches present the highest errors (both systematic and random). This is to be expected since these elements are nearly always in the elastic domain (with a stress magnitude lower than 200 MPa), thus the signal to noise ratio is not favourable. Moreover, this figures shows that the errors near the localization bands are lower than $10\,\%^{\pm 5\,\%}$. This is to be expected since

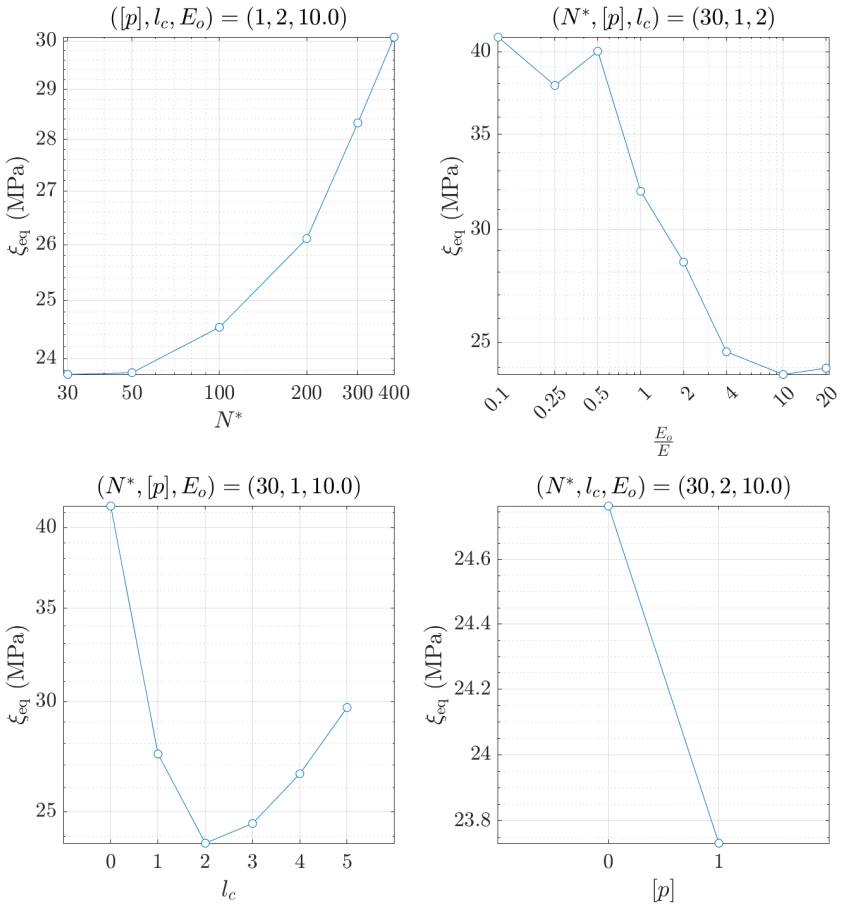

FIGURE 11 Evolution of ξ_{eq} with respect to the *DDI* parameters. Note that the y-scale differs from one figure to another.

in these regions plasticity occurs and thus where high stress magnitudes are obtained.

Another space of interest is the $\{||\varepsilon||_{VM}, ||\sigma||_{VM}\}$ space since it is the most commonly used one for the characterization of materials. Figures 15a and 15b respectively depict the distribution of the filtered mechanical points in the considered space and the stress errors associated. These figures support the observations made when analyzing Figure 13. Indeed, the errors are lowest for mechanical states that are highly redundant and when plasticity occurs. Under these circumstances, the errors are below 5 %. In addition, despite the amount of data available during elasticity, due to the unfavourable signal to noise ratio, high relative errors are obtained.

It is also of interest to consider the *DDI* relative error distribution in the $\{I_1, ||\sigma||_{VM}\}$ space. Indeed this space can be used to assess the multiaxiality achieved wihtin the sample during the experiment. Figures 16a and 16b respectively depict the distribution of the filtered mechanical points in the considered space and the stress errors associated. The distribution shows that despite the introduction of a central hole and notches, most of the mechanical points are in a state close to a uniaxial tension one. Some uniaxial compression states are reached, but the stress amplitudes reached are not sufficiently high enough to ensure a favorable signal to noise ration. Thus, the stress errors remain higher than 20 % for the points under uniaxial compression. Furthermore, this figure shows that the mechanical points leading to the lowest error are obtained for the higher stress magnitudes (as already evidenced with the previous figures) and that these points are under mainly uniaxial tension.

At last but not least, let us consider the *DDI* method ability to retrieve the strain-rate dependency of the reference stress fields. Indeed, let us recall that the stress fields used to initialize the method have a different strain-rate dependency than the sought ones. For this purpose stress-strain curves can be plotted for different average strain-rates. To plot such a figure, the average strain-rate over time for each element is computed.

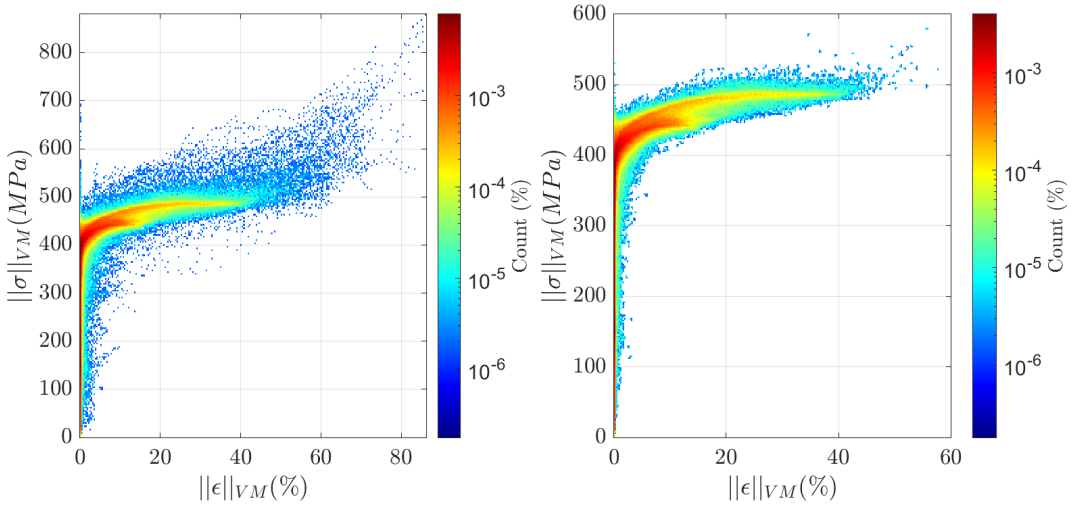

(a) Mechanical points distribution in the $\{||\epsilon||_{VM}, ||\sigma||_{VM}\}$ space.

(b) Mechanical points distribution in the $\{||\epsilon||_{VM}, ||\sigma||_{VM}\}$ space after the *a posteriori* filtering.

FIGURE 12 Mechanical points distribution in the $\{||\epsilon||_{VM}, ||\sigma||_{VM}\}$ space before and after the use of the filtering operator.

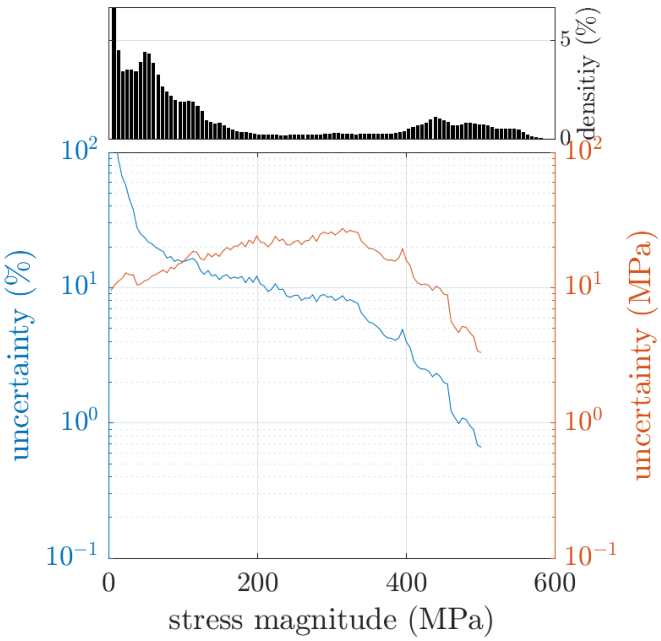

FIGURE 13 Stress uncertainty with respect to the stress magnitude. The distribution of the stress magnitude is given by the histogram while the blue and red lines are respectively the relative and absolute values of the stress uncertainty.

Then, using a clustering algorithm (here k-means), these average strain-rates are regrouped in 20 clusters. The stress-strain curves are then obtained by averaging the stresses and strains for each cluster. Figure 17 then shows the relative errors at $||\epsilon||_{VM} = 0.05$, 0.10 and 0.15 for the 20 average strain-rates. The dashed lines depict the FE solution using model B, while the stars depict the *DDI* solution. This figure confirms that model A and the model B have different strain-rate dependencies. Indeed, the relative error of the initialization stress fields increases with the strain-rate for all the strain levels considered. Furthermore, this figure evidences that the *DDI* method is able to retrieve the sought strain-rate dependency despite the initialization. This is supported by the fact that the relative error remains nearly constant below 6 %, for all the strain levels considered.

To summarize, by using kinematic fields from VID, one can assess the experimental accuracy that can be obtained using the Data-Driven Identification method for our sample geometry, loading conditions and camera. The conclusions are as follows:

- Below 200 MPa the signal to ratio is not favourable, due to the noise on the strain measurements. The related mechanical points are mainly during elasticity. Furthermore these points are mainly located above and below the hole and notches.
- Since the method proposed is data-based, the abundance of data leads to low stress errors. Indeed, when data is sufficiently abundant errors remains below 5 %.
- In the considered experiment most of the mechanical points are under a uniaxial tension state, despite the

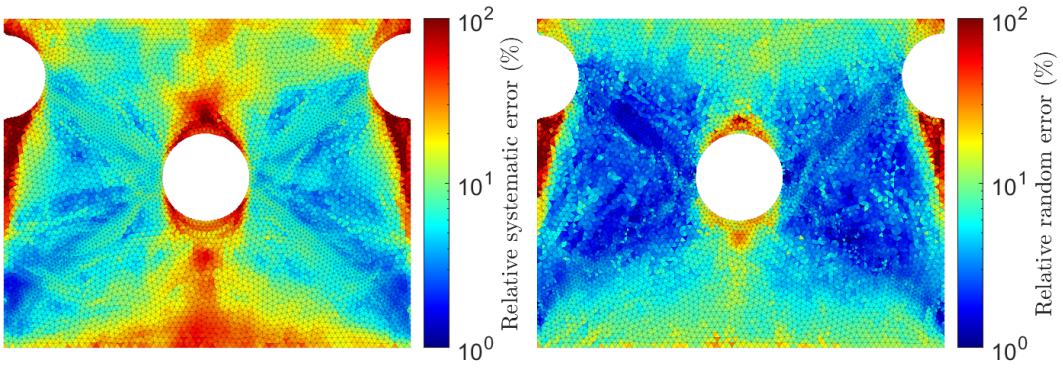

(a) Stress systematic error, **(b)** Stress random error,

FIGURE 14 Stress systematic and random error in the physical space.

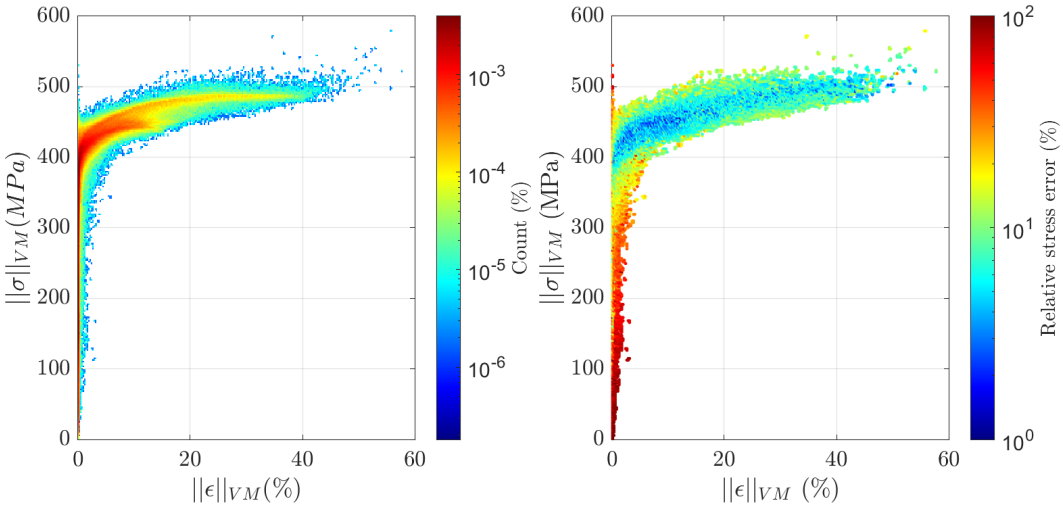

(a) Mechanical points distribution in the $\{||\varepsilon||_{VM}, ||\sigma||_{VM}\}$ space,

(b) Stress relative error in the $\{||\varepsilon||_{VM}, ||\sigma||_{VM}\}$ space,

FIGURE 15 Mechanical points distribution and stress relative errors obtained in the $\{||\varepsilon||_{VM}, ||\sigma||_{VM}\}$ space.

geometry considered. These points are located in the vicinity of the localization bands obtained.

- At last, the *DDI* method is able to retrieve the correct strain-rate dependency of the reference within 6 %. This illustrates the robustness of the method to its initialization.

5 | EXPERIMENTAL RESULTS AND DISCUSSIONS

5.1 | Evolution of macroscopic quantities during the test

The deconvolution between the distortions and the effective displacements is made using the camera model built using the 12 calibration shots. In addition, using the reference shot taken prior to the test, the changes of the extrinsic parameters can be taken into account. Finally, the correct pairing between the sensors and the mirror faces is identified using optical considerations ([36]). This allows the displacement, strain and strain-rate fields to be extracted.

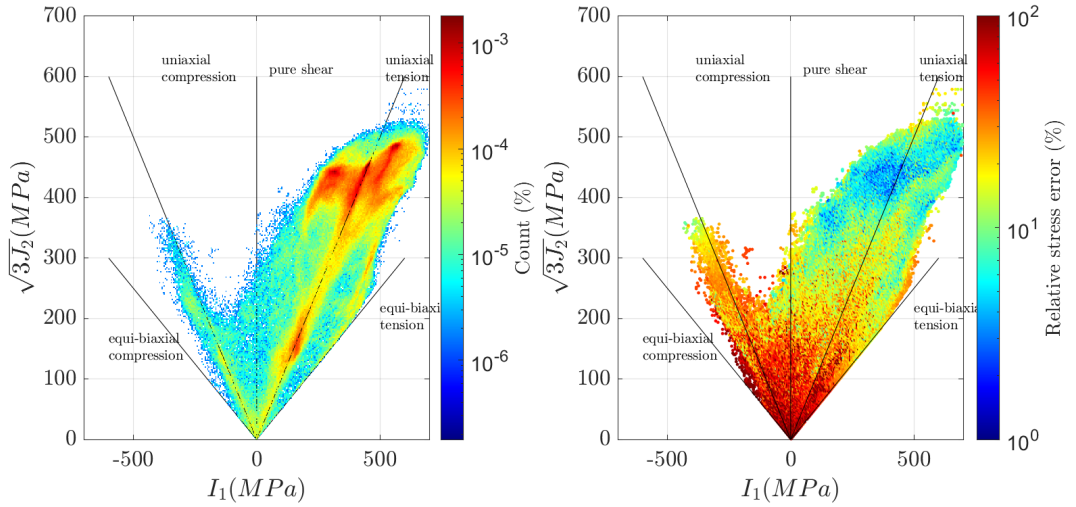

(a) Mechanical points distribution in the $\{I_1, ||\sigma||_{VM}\}$ space,

(b) Stress relative error in the $\{I_1, ||\sigma||_{VM}\}$ space,

FIGURE 16 Mechanical points distribution and stress relative errors obtained in the $\{I_1, ||\sigma||_{VM}\}$ space.

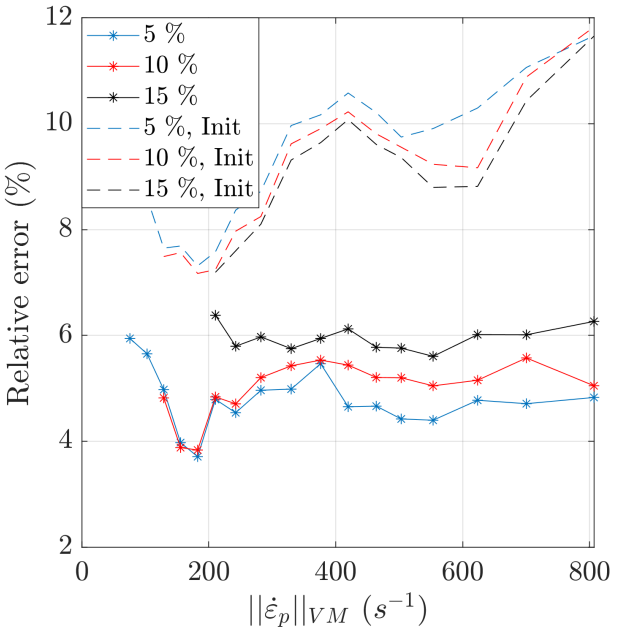

FIGURE 17 Relative stress error evolution with respect to the strain-rate, computed for different strain levels. The stars represent the results obtained with the *DDI* while the dashed lines are those obtained with the FE initialization using model B.

Figure 18 depicts the evolution of different quantities of interest during the experiment.

First, let us look at the temporal evolution of the averaged axial displacement and velocity obtained in the whole sample (depicted by the simple lines) and of the nodes located at the bottom of the mesh (depicted by the lines with markers), *i.e.* close to the sample head where the loading is applied. Figure 18a shows displacement in blue and velocity in red. The three vertical dashed lines are the time steps for which associated fields will be discussed later-on. Note that the zero in the timeline correspond to the time when the Cordin-580 is triggered by the load cell, hence the negative times for the first images. The loading of the specimen induces immediately on the loaded edge a displacement ramp, reaching about 2.8 mm before the initiation of the crack. The averaged axial displacement in the whole sample has a similar behaviour, with a lower slope, and reaches about 2 mm. The velocities in the whole sample or for the nodes at the bottom of the mesh have the same trend. The velocities evidence two stages: from the beginning to approximately t = 370 µs the velocities increase in the tension direction, then from t = 370 µs to t = 620 µs they decrease. The second stage can be explained by considering the possibility that the contact between the sliding bar and its enclosing case is not permanent. Indeed, if the sample goes faster than the actuator, then when there is no more contact its speed will naturally decrease until there is contact again. One way to verify this hypothesis would have been to record accurately the speed of the actuator (using DIC with a high speed camera for instance). However, this was not done for these experiments. During the experiment, the maximum speed reached on the loaded edge is about 4.8 m s^{-1} in about 476 µs which represent an acceleration on the order of 1×10^4 m s^{-2}; while the

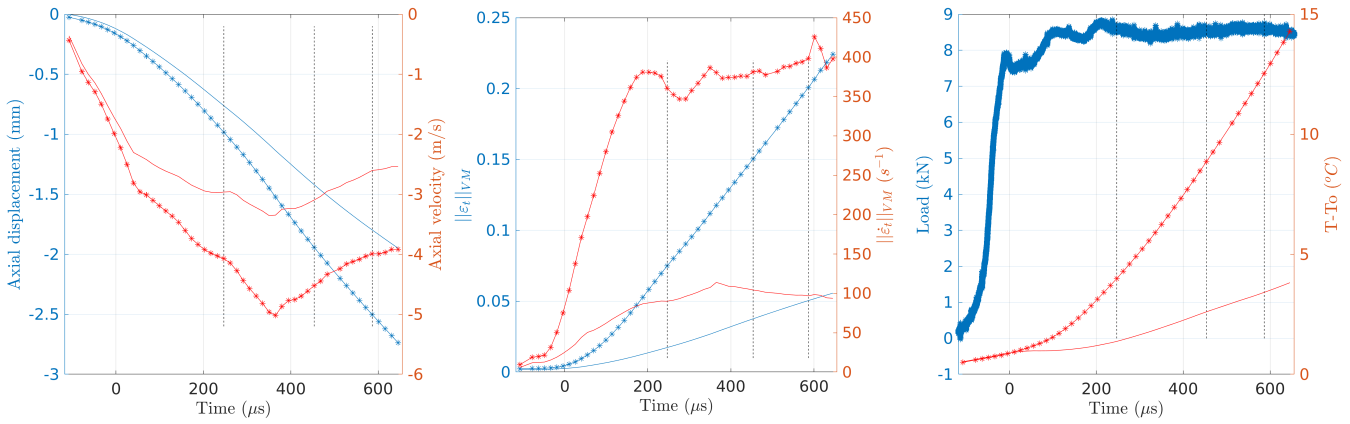

(a) Average U_y and V_y, **(b)** Average total strain and strain-rates, **(c)** Average temperature raise and load,

FIGURE 18 Evolution of different quantities of interest during an heterogeneous test. A simple line denotes the evolution of the considered quantity averaged in the whole sample, while a line with marker denotes its evolution in a particular zone (either the bottom of the mesh or the localization band).

maximum speed experienced by the whole sample is about $3.5\,\mathrm{m\,s^{-1}}$.

Figure 18b plots the evolution of the Von-Mises norm of both the total strain (in blue) and total strain-rates (in red) either in the whole sample (depicted by the simple lines) or in a localization band during the experiment (depicted by the lines with markers). This figure shows that during the first 100 µs of the experiment, the sample is mainly in an elastic regime ($||\varepsilon_t||_{VM} \leq 0.005$). Furthermore, the total strain in the localization band goes past 0.01 after about 150 µs, after which it increases following a ramp until about 0.22 before the crack initiation. On the other hand, the global total strain reaches only 0.05 before the crack initiation, which shows that deformation mainly occurs in the localization bands. In the considered band, two stages of the normalized total strain-rate can be observed. First, it ramps up to $375\,\mathrm{s^{-1}}$ in about 300 µs. Then, the normalized total strain-rate reaches a plateau and oscillates between $350\,\mathrm{s^{-1}}$ and $400\,\mathrm{s^{-1}}$. Similarly to the total strain, the total strain-rate in the whole sample is lower than the one observed in the bands as it reaches only $100\,\mathrm{s^{-1}}$.

At last, Figure 18c shows the evolution of the load during the experiment (in blue). It also depicts – for information purpose only – the average temperature increase (in red) either in the whole sample (depicted by the simple line) or in the considered band (depicted by the line with markers). Two stages can be evidenced for the load. During the first 150 µs the load ramps up until 8 kN. Then it reaches a plateau and oscillates around 8.5 kN. Considering an initial cross section S_0 equal to $1.68 \times 10^{-5}\,\mathrm{m^2}$ (subtracting the holes), the engineering stress can be estimated at 500 MPa. This value is in line with the ones obtained in [12]. A slight increase of temperature of about 0.3 °C is observed while the sample should slightly cool down by the same amount due to thermoelasticity. This observation is explained by the fact that the dedicated calibration procedure applied to retrieve temperature fields is not is not reproducible enough to entirely get ride of small variations, and thus does not allow to capture thermoelasticity. However, note that thermoelasticity would have been almost impossible to capture anyway when considering the measurement uncertainty achieved with the procedure used (300 mK), which is already in the same order of magnitude as thermoelastic effects. Nevertheless, after 100 µs, the temperature increases follow the same trend as the normalized total strains, as expected. The sample temperature increase reaches 15 °C on average in the localization band before crack initiation with a rate on the order of 25 K/ms. On the other hand, the temperature increase in the whole sample reaches about 4 °C before crack initiation.

5.2 | Displacement and strain fields

Figure 19 shows sample images, displacement fields in both directions, the axial strain fields for the three time steps introduced previously. The displacement fields obtained are consistent with a tensile test. The first two images underline the fact that the tensile test is not perfectly axial. Indeed, the axial displacements are higher on the left-hand side of the sample. This phenomenon was observed for all the experiments performed as well as on the preliminary tests. In turn, crack initiation systematically begins on the left-hand side of the sample before the right-hand side. No clear explanations have been found for

this observation. It may be partly due to the fact that the sample is already pre-constrained, and a non-planar contact between the sliding bar and its enclosing case may also come into play. However, no clear evidences have been found to confirm these hypotheses. The strain fields at 246.79 µs further confirm the fact that the load imposed on the sample is not symmetrical since strains are higher in the left band. The sample geometry induces localization bands as predicted by the FE simulations with little strain everywhere else.

In addition, strain and strain-rate ranges experienced by the sample during the test is investigated. To this effect, Figure 20 depicts the strain *versus* strain-rate occurrences that are observed through the chosen ROI during the whole test. White areas represent states that the sample never reached. This figure shows that most of the sample during the experiment undergoes small strain as well as plastic strain-rates. This is consistent with the strain fields obtained. Furthermore, let us note that before cracking, only a few points reach a total strain higher than 0.25. The strain and strain-rates in the range of respectively $[0 - 0.25]$ and $[0\,\mathrm{s}^{-1} - 500\,\mathrm{s}^{-1}]$ predicted by the numerical twin are recovered quite nicely.

5.3 | DDI experimental application to the XES characterization campaign

Stress fields

The *DDI* algorithm has been presented and then applied to a numerical test case in the previous section. Now the proposed method will be applied to the data obtained during the XES characterization campaign. The performance of the proposed methodology will be discussed as well as the intrinsic limitations of the method, of the material as well as the geometry chosen.

The experimental procedure for the *DDI* is very similar to the one presented in Fig. 10. In this case, the experimental data replace the ones obtained from the first simulation of the numerical test case. The load that will be used to rescale the load profile is the one captured by the load cell during the dynamic tensile test adjusted following the method presented in Section 3. Furthermore, as the *DDI* requires two FE simulations to be performed, the material model chosen for the initialization is the Johnson-Cook model and the parameters used are the one identified on the raw data from ONERA (*i.e.* the model A from the numerical test case). At last, the method's parameters are the ones considered optimal from the numerical twin study, *i.e.* $N^* = 30$, $E_o = 10.0 \cdot E$, $l_c = 2$ and $[p] = [w]$. Additionally, the same *a posteriori* filtering operator will be applied on the results. Hence, all the results presented in what follows are obtained using these parameters and the filter defined in Section 4.

Once the *DDI* algorithm applied, the mechanical and material states are available. From these states the Von-Mises norm of the stresses can be obtained. Figure 21 depicts the spatial cartographies of respectively the total strains and the Von-Mises stresses for three different time steps. The cartography of the Von-Mises stresses of the last image (Fig. 21f) shows that, as expected, the notches and the central hole create stress concentration bands. In these bands the Von-Mises stresses reach about 500 MPa. In addition, in the secondary bands, the stress is about 400 MPa. Above and below the central hole and the notches the stress magnitudes remain below 200 MPa. These observations are consistent with the numerical study performed.

Let us recall that the experiment was designed to provide different loading paths of the material and wide spectra of strain and strain-rates during a single test. Hence, Figure 22 enables the verification of these specifications. Figure 22a depicts the stress distribution in the space $(I_1, \|\boldsymbol{\sigma}\|_{VM})$ for the selected mechanical states. It follows that this figure is an indicator of the stress triaxiality that occurs during the experiment. This figure shows that the sample is mainly under an uniaxial tensile state. However, some compression and shear states are reached within the specimen. In addition, Figure 22b shows that the strain and strain-rate spectra mainly seen by the specimen are $[0 - 0.18]$ and $[0\,\mathrm{s}^{-1} - 450\,\mathrm{s}^{-1}]$. Nevertheless, some regions of the sample reach higher strain and higher strain rate values. In order to associate these states to a region in the sample, several elements located at different regions of interest of the sample are selected (see Fig. 22c). The loading paths of these elements are depicted in the previous figures considered. As it can be expected, the region above and below the hole (and by extension the notches) are under a compressive state. Moreover, as expected the elements in the band are mainly in a uniaxial tensile state. Figure 22b clearly highlights that the different regions of the bands are under different but quasi-constant strain-rates. This further justifies the specimen geometry since it clearly demonstrates that at least the results of uniaxial tensile tests performed at different strain-rates can be retrieved.

Material behaviour of the XES steel: comparison with the reference data

By construction, the material states best fit the behaviour of the material. Figure 23a depicts a projection of the material states. The black and red lines are the raw data from previous characterization of the XES steel performed at ONERA. Let us also note that even after the selection of the clusters, some material states with singular behaviours are remaining. However, most of the material states remaining are still representative of the behaviour of the material. Indeed, the behaviour of the material at $70\,\mathrm{s}^{-1}$ from previous characterization is for instance well

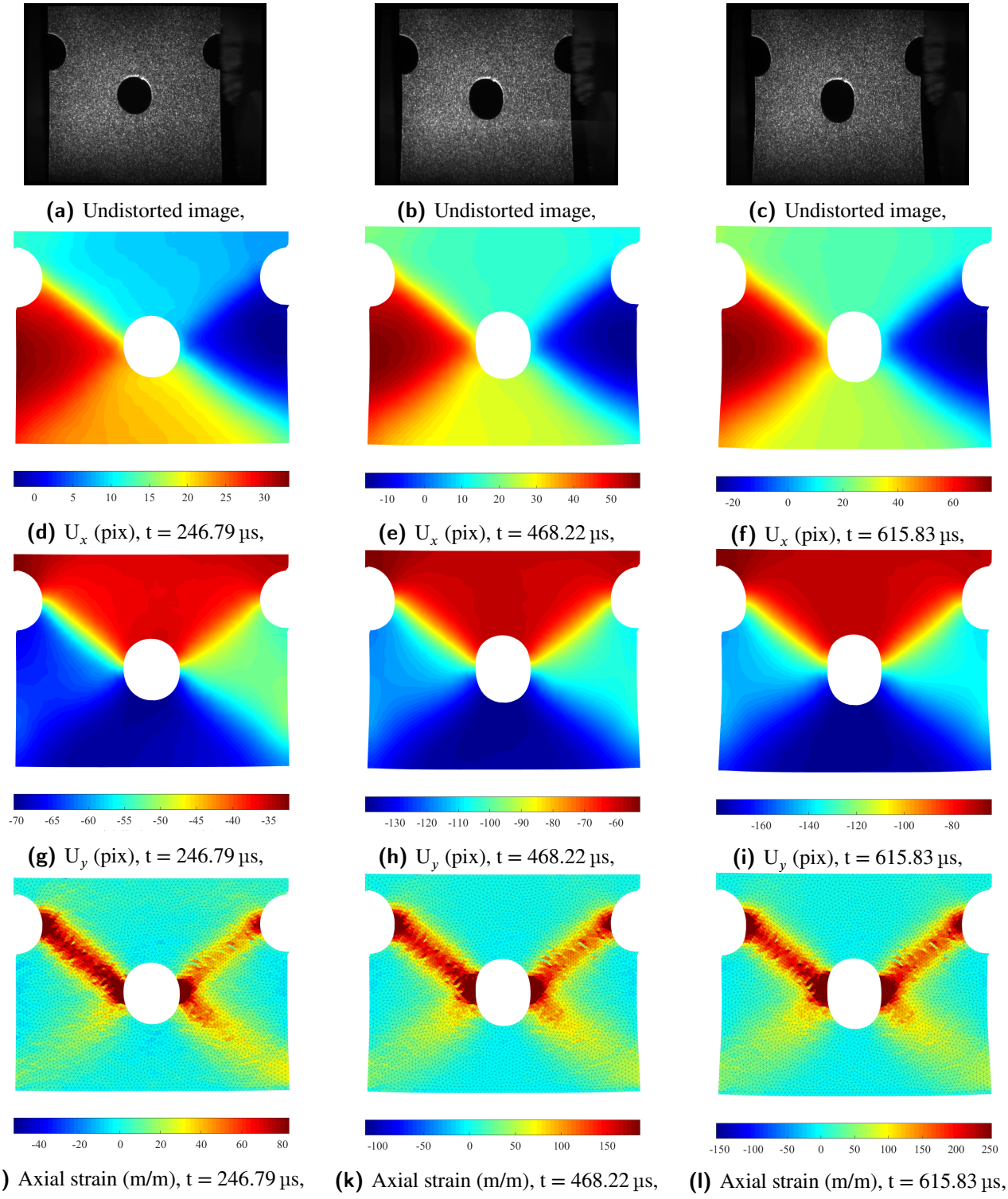

(a) Undistorted image, **(b)** Undistorted image, **(c)** Undistorted image,

(d) U_x (pix), t = 246.79 µs, **(e)** U_x (pix), t = 468.22 µs, **(f)** U_x (pix), t = 615.83 µs,

(g) U_y (pix), t = 246.79 µs, **(h)** U_y (pix), t = 468.22 µs, **(i)** U_y (pix), t = 615.83 µs,

(j) Axial strain (m/m), t = 246.79 µs, **(k)** Axial strain (m/m), t = 468.22 µs, **(l)** Axial strain (m/m), t = 615.83 µs,

FIGURE 19 Undistorted images, displacement fields, strain fields obtained during a dynamic tensile test, for different time steps.

captured by the *DDI* method, in the same range of strain-rate (see the colour). This also confirms the fact that the material considered in this study, known to be strain-rate dependent, has a dependency which fades at about 100 s^{-1}. Indeed, the stress response variation from 100 s^{-1} to 500 s^{-1} is more packed than from 1 s^{-1} to 70 s^{-1}.

Moreover, Figure 23b shows 10 stress-strain curves obtained for different averaged strain-rates, and the reference data are

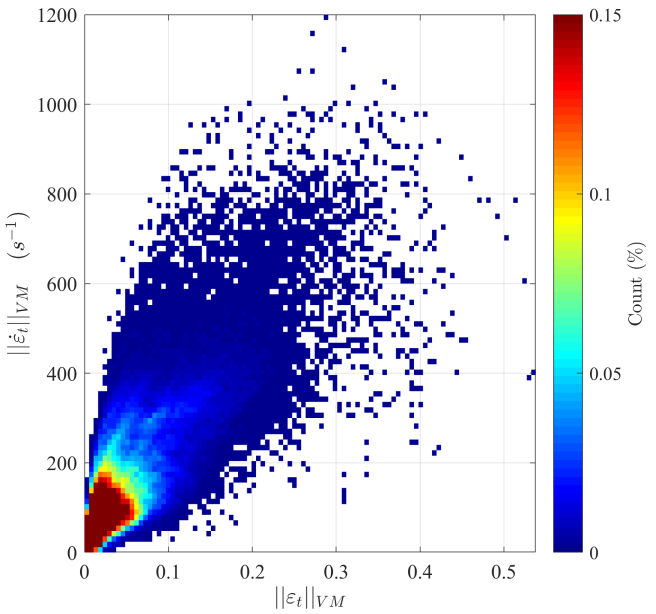

FIGURE 20 Von-Mises norm of the strain vs Von-Mises norm of the strain-rates distribution obtained during the experiment, prior to crack initiation. The colour corresponds to a 2D histogram plot. The count per bin is normalized by the number of element in the ROI multiplied by the number of time steps. The strain states that were never experienced by the sample remain white.

depicted by the dashed lines. The grey area around the dashed line represent a relative error of $\pm$ 6 %. This figure shows that the data obtained for an average strain-rate of 81 s^{-1} is in line with the reference data at 70 s^{-1} when taking into account the relative error. Indeed, when taking into account the uncertainty on the stress estimation from Section 4, the data from 80 s^{-1} to 191 s^{-1} are also in line with the reference data. In particular, the initial yield stresses as well as the hardening modulus obtained at these strain-rates are in line with the reference data. The figure also allows to confirm the fact that the strain-rate dependency fades off around 100 s^{-1}, and also confirms a softening of the material response for strains below 0.05 (see Fig. 24a). Furthermore, this figure can be compared to the stress-strain curves obtained in the literature [12], that are recalled in Figure 24. While the *DDI* stress estimations are in line with our reference data from [26], they differ slightly from the ones in Fig. 24a. Indeed, while we observe (using *DDI*) a saturation of the yield stress and hardening at about 191 s^{-1} with a stress peak near 500 MPa, data obtained from [12] at 200 s^{-1}, 360 s^{-1} and 440 s^{-1} show an increase of the peak stress up to 600 MPa followed by a massive softening. Nevertheless, Fig. 24b highlights the difficulty to have consistent results with different experimental apparatus at high strain-rates. Indeed, by using different techniques, the stress obtained at a plastic strain of 0.1 at a strain-rate of 500 s^{-1} has an uncertainty of about 50 MPa which represent a relative error of about 10 %. Regarding Figure 24b, one sees that our *DDI* results are closer to data obtained on SHPB or using the special apparatus designed by Haugou [12]. While the question of the reproducibility of the data using different experimental apparatus remains open, Figure 23b shows that *DDI* and a dedicated sample geometry allows to accurately capture, with a single apparatus, consistent elasto-plastic data from 30 s^{-1} to about 250 s^{-1}.

The material states obtained using this *DDI* method can also be compared to the stresses predicted by the modified Krupkowsky model that better fits the non-linear strain-rate dependency of the XES steel than the Johnson-Cook model. Since neither the material states nor the direct estimation of Krupkowsky stress from experimental strains and strain-rates will verify the equilibrium, the comparison can be considered as fair. Hence, Figure 25 displays three cartographies of the difference between the stresses predicted by Krupkowsky and the material states: the first one is in the $(\|\boldsymbol{\varepsilon}\|_{VM}, \|\dot{\boldsymbol{\varepsilon}}\|_{VM})$ space. The second one depicts the discrepancy but in the stress invariant space while the last one is in the $(\|\boldsymbol{\varepsilon}\|_{VM}, \|\boldsymbol{\sigma}\|_{VM})$ space. It can be observed on the first cartography that the stress discrepancies are mainly higher than 10 % for low values of strain combined with high values of strain-rates. As it was shown earlier with Figure 22, these states are mainly experienced by the elements near the hole, and thus the strain-rates and stress values have to be taken with precautions. In addition, these states are also associated with few clusters of data, which also explains the significant discrepancy. Let us note that apart from the these states, the discrepancies remain within the accuracy interval observed for states subjected to uniaxial tension in Section 4 which further comforts the relevance of the *DDI* stress estimations. Furthermore, the cartography of the difference between the prediction using the modified Krupkowsky model and the *DDI* results in the stress invariant space is in quite good agreement with the one obtained in Section 4. Indeed, this figure shows that the *DDI* method is able to match the predictions from the constitutive model when the material is under uniaxial tension, within a relative discrepancy of about 5 %. Moreover, since the modified Krupkowsky model describes the plastic flow, it is not able to predict stresses in elasticity. This is why the errors obtained are higher than 50 % for values of stress lower than 200 MPa. This is supported by the cartography of the relative error in the $(\|\boldsymbol{\varepsilon}\|_{VM}, \|\boldsymbol{\sigma}\|_{VM})$ space. The errors are significant for elasticity. Nevertheless, during plasticity, the errors remain under 10 %. All these results comfort the fact that the modified Krupkowsky

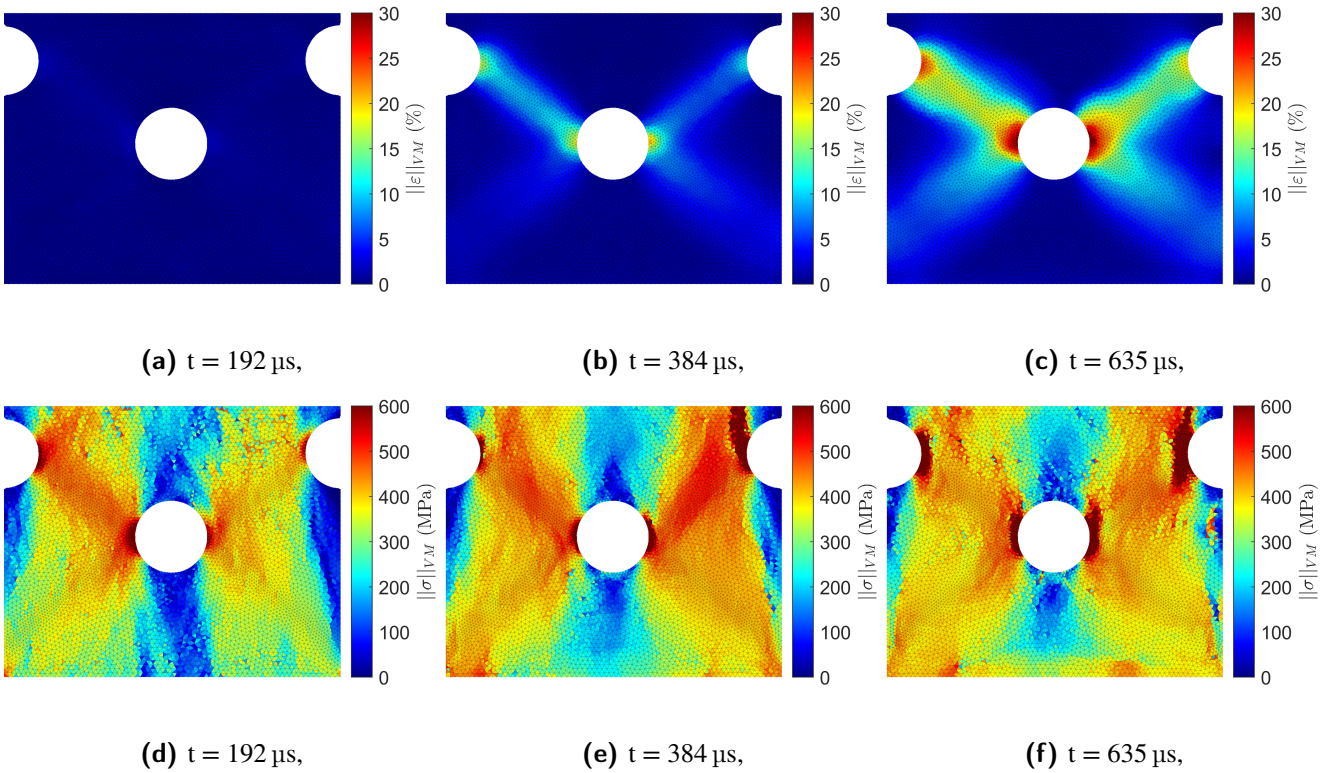

(a) t = 192 µs, **(b)** t = 384 µs, **(c)** t = 635 µs,

(d) t = 192 µs, **(e)** t = 384 µs, **(f)** t = 635 µs,

FIGURE 21 Cartographies of the Von-Mises norm of the total strains and stresses for three different time steps.

model, even calibrated over 3 uniaxial curves, is able to extrapolate well at higher strain-rates and when we slightly deviate from its validity loading configuration domain.

Furthermore, the material states obtained with the *DDI* can be used in a more conventional way to identify constitutive parameters. Parameters are identified using the selected material states obtained in this work. Since these states do not contain quasi-static data, the quasi-static data from ONERA is also taken into account, in order to ensure that the parameters identified characterize the material from quasi-statics to high strain-rates. The identification is performed for strains higher than 0.01. The parameters obtained are presented in Tab. 8, which also recall the parameters from [12]. Strong variations are observed in particular for exponent c. In addition, ϵ_0, $\dot{\epsilon}_0$ and b, which capture the strain-rate dependency, also differ significantly from the reference parameters ($\geq 15\,\%$). Nevertheless, by checking the discrepancies between reference data from ONERA and the modified Krupkowsky model based on the updated parameters using *DDI* stresses (see Fig 26), one observes that the reference data are captured within 6 % of relative error for the quasi-static response and the one at $70\,s^{-1}$. In addition, the data are captured within 5 % for the intermediate response ($0.67\,s^{-1}$). Since the data from the intermediate response were not included in the parameters identification process, this demonstrates the extrapolation ability of the considered model. In addition, this indicates that the model has a weak sensitivity to its parameters, and also that its 7 parameters can be recovered from only 2 tests: a quasi-static one, and a heterogeneous and high strain-rates one.

To summarize, the *DDI* method has been applied to the experimental data obtained in Section 3. The stresses have been reconstructed. The stress distribution confirms that the sample is mainly under uniaxial tension during the experiment, but some regions are under compression and shear (the region above and below the hole and notches for instance). The strain and strain-rate spectra that the sample is submitted to are [0 – 0.18] and [$0\,s^{-1}$ – $500\,s^{-1}$]. Furthermore, the *DDI* algorithm is able to retrieve the behaviour identified during previous characterization campaigns. In particular, using the material states and data from a simple quasi-static test, constitutive parameters can be identified for the modified Krupkowsky model, which allow to retrieve the behaviour with a relative error below 10 % for strain-rates from $0.01\,s^{-1}$ to a few hundreds of s^{-1}. At last but not least, based on the accuracy assessment performed in the previous section and a comparison with the predictions of the modified Krupkowsky model, this model's stress predictions can be considered with confidence even when extrapolated for higher strain-rates than the ones used to calibrate it.

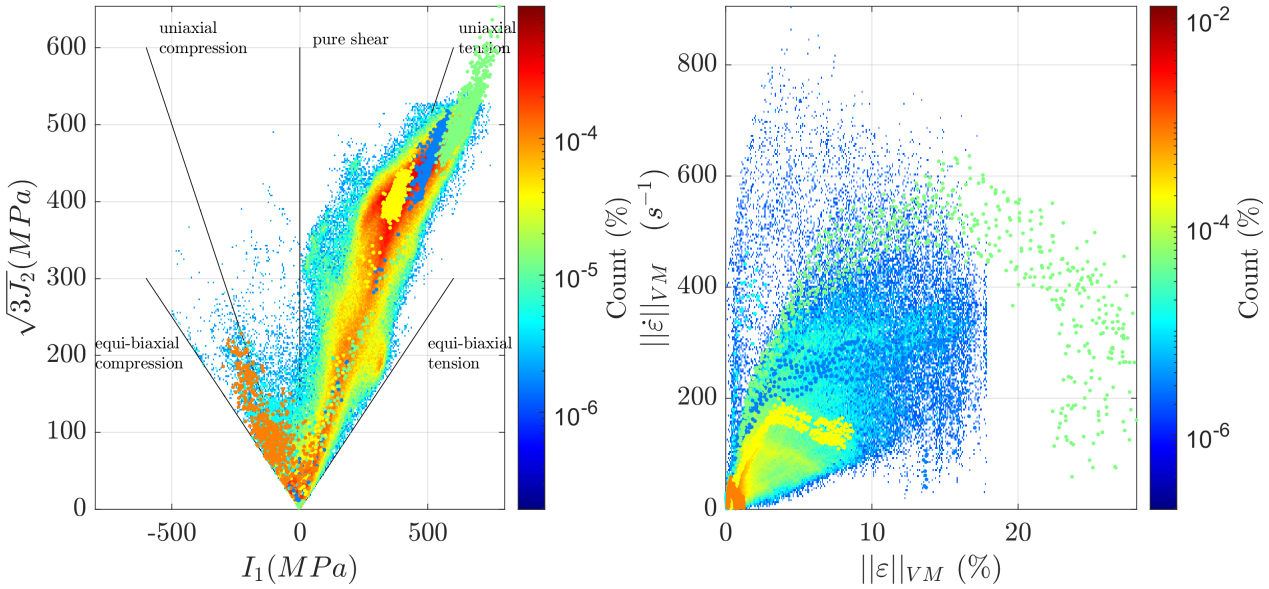

(a) Stress distribution with the loading path of selected elements,

(b) Strain and strain-rate distribution with the loading path of selected elements,

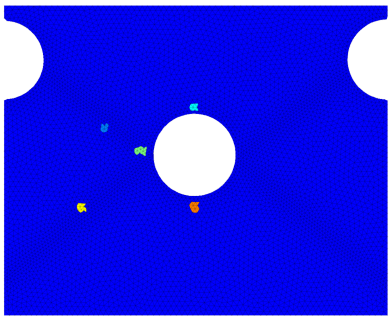

(c) DDI mesh and localization of the selected elements,

FIGURE 22 Stress distribution, strain and strain-rate distributions during the experiment for the selected mechanical states. The loading paths of a few selected elements are superimposed on these distributions.

Parameters	K (MPa)	ε_0	n	$\dot{\varepsilon}_0$ (s^{-1})	a	b	c
Section 3	526.6	0.024	0.221	0.085	0.0002	0.385	0.002
This work + QS data	512.8	0.0281	0.2233	0.0705	0.0002	0.3361	0.0002
Relative variation (%)	2.62 %	−17.00 %	−1.04 %	17.04 %	90 %	12.71 %	90 %

TABLE 8 Comparison of the modified Krupkowsky model parameters identified using data from [26] or from this work combined with quasi-static data from ONERA.

6 | CONCLUSIONS AND PERSPECTIVES

In this paper, the Data-Driven Identification method is presented. Its accuracy has been assessed using a numerical twin. Then, a pre-notched sample with a central hole has been subjected to a high speed tensile test. Fullfield kinematic data have been obtained and quantitatively captured the events during the test. At last, these fullfield kinematic fields have been

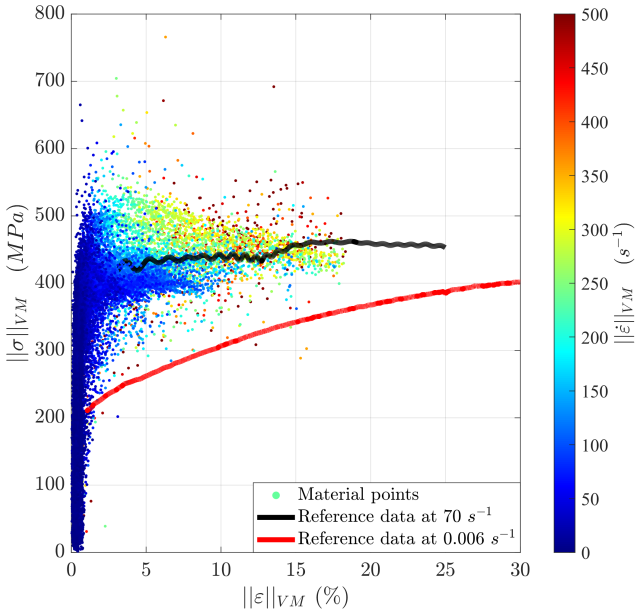

(a) Material states in $(\|\boldsymbol{\varepsilon}\|_{VM}, \|\boldsymbol{\sigma}\|_{VM})$. The colour of the markers denote the strain-rates, while the lines denote the reference data from ONERA,

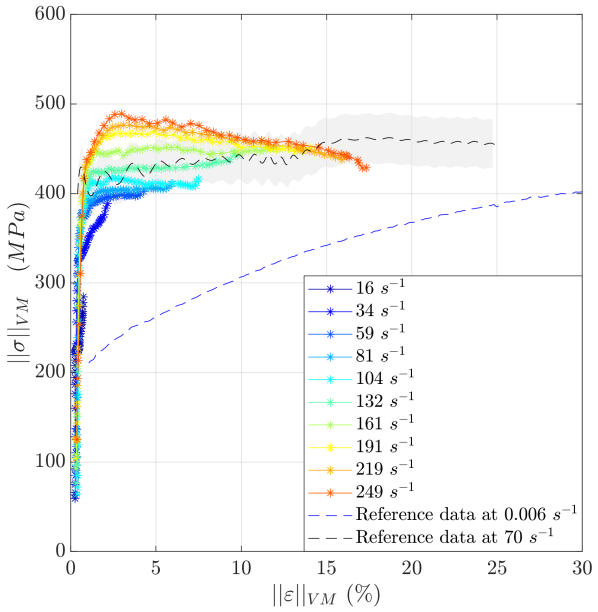

(b) Stress-strain curves for different averaged strain-rates extracted from the selected material states during one experiment,

FIGURE 23 Material states in the space$(\|\boldsymbol{\varepsilon}\|_{VM}, \|\boldsymbol{\sigma}\|_{VM})$ as well as stress-strain curves for different averaged strain-rates obtained during one experiment.

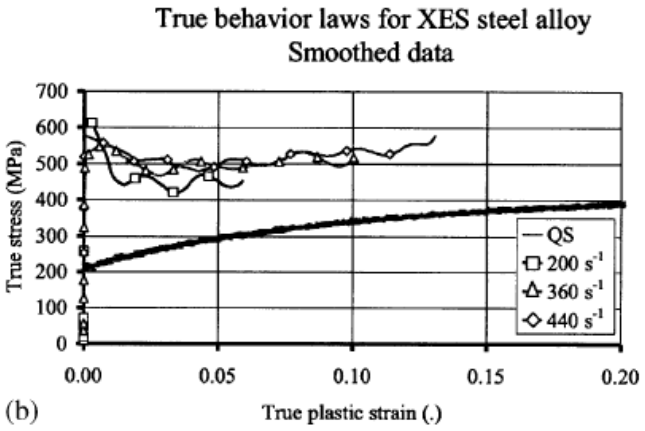

(a) Stress-strain curves obtained for the XES for different strain-rates from [12],

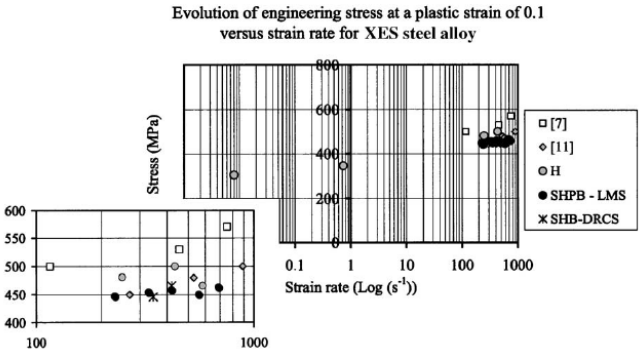

(b) Evolution of the stress at a plastic strain of 0.1 in function of the strain-rate using different techniques, from [12],

FIGURE 24 XES characterization data from [12] and comparison of the results obtained using different experimental techniques.

used as input for the *DDI* to estimate stress fields during the experiment. The main conclusions are as follows:

- The parameters of the *DDI* method play an important role in the stress reconstruction. The analysis performed on the numerical test case lead to the selection of these parameters.

- The numerical test case illustrates the ability of the proposed methodology to retrieve the material behaviour despite the use of a wrong set of constitutive parameters as initialization. It showed in particular that the algorithm is able to retrieve the material's strain-rate dependency accurately.

- Using the results from Virtual Image Deformation, the impact of noise on the stress estimation can be assessed.

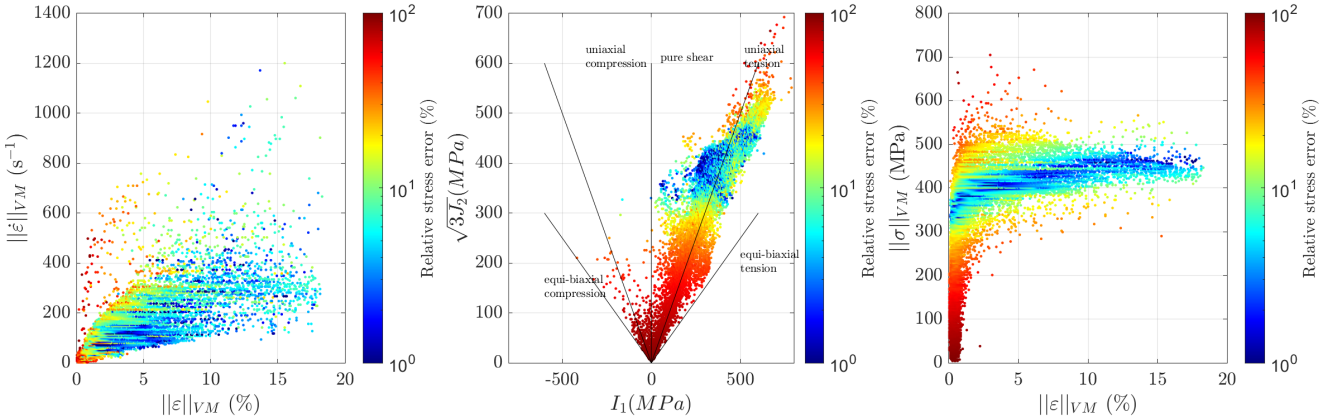

(a) Cartography of the relative error in $(\|\boldsymbol{\varepsilon}\|_{VM}, \|\dot{\boldsymbol{\varepsilon}}\|_{VM})$, **(b)** Cartography of the relative error in the stress invariant space, **(c)** Cartography of the relative error in $(\|\boldsymbol{\varepsilon}\|_{VM}, \|\boldsymbol{\sigma}\|_{VM})$,

FIGURE 25 Comparison between the stress predictions using the modified Krupkowsky model and the material states from the *DDI*.

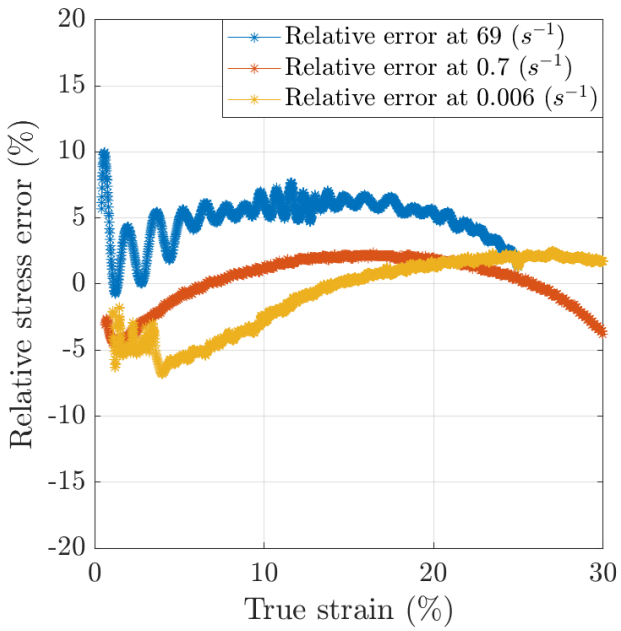

FIGURE 26 Relative errors between the reference data and the fit using the identified parameters.

An accuracy of $10\,\%^{\pm 5\,\%}$ is obtained on the stress estimation. At last, using the *DDI* Data to perform identification leads to relative errors lower than 5 %.

- The application of the proposed method to the experimental data allows estimating stress fields. The material behaviour captured by the material states are consistent with the data obtained at ONERA during previous experimental campaigns. In the presented study, the stress are retrieved with confidence for strains and strain-rates in the range of [0.01 – 0.18] and [10 s^{-1} – 500 s^{-1}].
- By combining the data from this work and data from a simple quasi-static test, constitutive parameters can be identified. These parameters are able to correctly retrieve the behaviour of the material over several strain-rates decades, with a relative error that remains below 5 %.

ACKNOWLEDGEMENTS

The support of Région Pays de la Loire, Nantes Métropole and European Union through grant Connect Talent IDS is gratefully acknowledged. The support of ANR through grant ANR-16-CE30-0007-01 is also gratefully acknowledged. Finally the authors would like to acknowledge all the colleagues and PhD students contributing to the informal working group, *OutLaw*, at GeM, especially Adrien Leygue and Raphael Langlois for the fruit-full discussions and their recent developments in rate-dependent *DDI*.

References

[1] Badaloni, M., M. Rossi, G. Chiappini, P. Lava, and D. Debruyne, 2015: Impact of experimental uncertainties on the identification of mechanical material

properties using DIC. *Experimental Mechanics*, **55**, no. 8, 1411–1426, doi:10.1007/s11340-015-0039-8.
URL http://link.springer.com/10.1007/s11340-015-0039-8

[2] Bouda, P., B. Langrand, D. Notta-Cuvier, E. Markiewicz, and F. Pierron, 2019: A computational approach to design new tests for viscoplasticity characterization at high strain-rates. *Computanional Mechanics*, **64**, no. 6, 1639–1654, doi:10.1007/s00466-019-01742-y.
URL http://link.springer.com/10.1007/s00466-019-01742-y

[3] Cameron, B. C. and C. Tasan, 2021: Full-field stress computation from measured deformation fields: A hyperbolic formulation. *Journal of the Mechanics and Physics of Solids*, **147**, 104186, doi:10.1016/j.jmps.2020.104186.
URL https://linkinghub.elsevier.com/retrieve/pii/S0022509620304130

[4] Dalémat, M., M. Coret, A. Leygue, and E. Verron, 2021: Robustness of the data-driven identification algorithm with incomplete input data, working paper or preprint.
URL https://hal.archives-ouvertes.fr/hal-03028848

[5] Dalémat, M., M. Coret, A. Leygue, and E. Verron, 2019: Measuring stress field without constitutive equation. *Mechanics of Materials*, **136**, 103087, doi:10.1016/j.mechmat.2019.103087.
URL https://linkinghub.elsevier.com/retrieve/pii/S0167663619302376

[6] Eggersmann, R., T. Kirchdoerfer, S. Reese, L. Stainier, and M. Ortiz, 2019: Model-Free Data-Driven inelasticity. *Computer Methods in Applied Mechanics and Engineering*, **350**, 81–99, doi:10.1016/j.cma.2019.02.016.
URL https://linkinghub.elsevier.com/retrieve/pii/S0045782519300878

[7] Fletcher, L., F. Davis, S. Dreuilhe, A. Marek, and F. Pierron, 2021: High strain rate elasto-plasticity identification using the image-based inertial impact (IBII) test part 1: Error quantification. *Strain*, **57**, no. 2, doi:10.1111/str.12375.
URL https://onlinelibrary.wiley.com/doi/10.1111/str.12375

[8] Fletcher, L. and F. Pierron, 2018: An image-based inertial impact (IBII) test for tungsten carbide cermets. *Journal of Dynamic Behavior of Materials*, **4**, no. 4, 481–504.

[9] — 2020: The Image-Based Inertial Release (IBIR) Test: A New High Strain Rate Test for Stiffness Strain-Rate Sensitivity Identification. *Experimental Mechanics*, **60**, no. 4, 493–508, doi:10.1007/s11340-019-00580-6.
URL http://link.springer.com/10.1007/s11340-019-00580-6

[10] Fletcher, L., J. Van-Blitterswyk, and F. Pierron, 2019: A novel image-based inertial impact test (IBII) for the transverse properties of composites at high strain rates. *Journal of Dynamic Behavior of Materials*, **5**, no. 1, 65–92.

[11] Gary, G. and W. K. Nowacki, 1994: Essai de cisaillement plan appliqué à des tôles minces. *Journal de Physique IV*, **04**, no. C8, C8–65–C8–70, doi:10.1051/jp4:1994809.
URL http://www.edpsciences.org/10.1051/jp4:1994809

[12] Haugou, G., E. Markiewicz, and J. Fabis, 2006: On the use of the non direct tensile loading on a classical split Hopkinson bar apparatus dedicated to sheet metal specimen characterisation. *International Journal of Impact Engineering*, **32**, no. 5, 778–798, doi:10.1016/j.ijimpeng.2005.07.015.
URL https://linkinghub.elsevier.com/retrieve/pii/S0734743X05001107

[13] Jones, E., J. Carroll, K. Karlson, S. Kramer, R. Lehoucq, P. Reu, and D. Turner, 2018: Parameter covariance and non-uniqueness in material model calibration using the Virtual Fields Method. *Computational Materials Science*, **152**, 268–290, doi:10.1016/j.commatsci.2018.05.037.
URL https://linkinghub.elsevier.com/retrieve/pii/S0927025618303501

[14] Kirchdoerfer, T. and M. Ortiz, 2016: Data-driven computational mechanics. *Computer Methods in Applied Mechanics and Engineering*, **304**, 81–101, doi:10.1016/j.cma.2016.02.001.
URL https://linkinghub.elsevier.com/retrieve/pii/S0045782516300238

[15] — 2017: Data Driven Computing with noisy material data sets. *Computer Methods in Applied Mechanics and Engineering*, **326**, 622–641, doi:10.1016/j.cma.2017.07.039.
URL https://linkinghub.elsevier.com/retrieve/pii/S0045782517304012

[16] — 2018: Data-driven computing in dynamics: Data-driven computing in dynamics. *International Journal for Numerical Methods in Engineering*, **113**, no. 11, 1697–1710, doi:10.1002/nme.5716.
URL https://onlinelibrary.wiley.com/doi/10.1002/nme.5716

[17] Klepaczko, J. R., H. V. Nguyen, and W. K. Nowacki, 1999: Quasi-static and dynamic shearing of sheet metals. *European Journal of Mechanics - A/Solids*, **18**, no.

2, 271–289, doi:10.1016/S0997-7538(99)80016-3.
URL https://linkinghub.elsevier.com/retrieve/pii/S0997753899800163

[18] Langlois, R., M. Coret, and J. Réthoré, 2022: Non-parametric stress field estimation for history-dependent materials: Application to ductile material exhibiting piobert–lüders localization bands. *Strain*, e12410.

[19] Langrand, B. and A. Combescure, 2004: Non-linear and failure behaviour of spotwelds: a "global" finite element and experiments in pure and mixed modes I/II. *International Journal of Solids and Structures*, **41**, no. 24-25, 6631–6646, doi:10.1016/j.ijsolstr.2004.06.009.
URL https://linkinghub.elsevier.com/retrieve/pii/S0020768304003245

[20] Langrand, B. and E. Markiewicz, 2010: Strain-rate dependence in spot welds: Non-linear behaviour and failure in pure and combined modes I/II. *International Journal of Impact Engineering*, **37**, no. 7, 792–805, doi:10.1016/j.ijimpeng.2010.01.004.
URL https://linkinghub.elsevier.com/retrieve/pii/S0734743X10000163

[21] LeBlanc, M. and D. Lassila, 1996: a hybrid technique for compression testing at intermediate strain rates. *Experimental Techniques*, **20**, no. 5, 21–24, doi:10.1111/j.1747-1567.1996.tb00459.x.
URL http://doi.wiley.com/10.1111/j.1747-1567.1996.tb00459.x

[22] Leygue, A., M. Coret, J. Réthoré, L. Stainier, and E. Verron, 2018: Data-based derivation of material response. *Computer Methods in Applied Mechanics and Engineering*, **331**, 184–196, doi:10.1016/j.cma.2017.11.013.
URL https://linkinghub.elsevier.com/retrieve/pii/S0045782517307156

[23] Leygue, A., R. Seghir, J. Réthoré, M. Coret, E. Verron, and L. Stainier, 2019: Non-parametric material state field extraction from full field measurements. *Computunational Mechanics*, **64**, no. 2, 501–509, doi:10.1007/s00466-019-01725-z.
URL http://link.springer.com/10.1007/s00466-019-01725-z

[24] Liu, C., 2021: Nonuniform Stress Field Determination Based on Deformation Measurement. *Journal of Applied Mechanics*, **88**, no. 7, 071005, doi:10.1115/1.4050535.
URL https://asmedigitalcollection.asme.org/appliedmechanics/article/88/7/071005/1104370/Nonuniform-Stress-Field-Determination-Based-on

[25] MacQueen, J. et al., 1967: Some methods for classification and analysis of multivariate observations. *Proceedings of the fifth Berkeley symposium on mathematical statistics and probability*, Oakland, CA, USA, volume 1, 281–297.

[26] Markiewicz, E., B. Langrand, N. Leconte, J. Fabis, and T. Dupuy, 2016: A methodology for the viscoplastic behaviour characterisation of spot-weld heat affected materials. *Journal of Materials Processing Technology*, **238**, 169–180, doi:10.1016/j.jmatprotec.2016.07.022.
URL https://linkinghub.elsevier.com/retrieve/pii/S0924013616302394

[27] Pierron, F. and L. Fletcher, 2019: Generalized stress–strain curves for IBII tests on isotropic and orthotropic materials. *Journal of Dynamic Behavior of Materials*, **5**, no. 2, 180–193, doi:10.1007/s40870-019-00197-9.
URL http://link.springer.com/10.1007/s40870-019-00197-9

[28] Pierron, F., H. Zhu, and C. Siviour, 2014: Beyond Hopkinson's bar. *Philosophical Transactions of the Royal Society A: Mathematical, Physical and Engineering Sciences*, **372**, no. 2023, 20130195–20130195, doi:10.1098/rsta.2013.0195.

[29] Platzer, A., A. Leygue, L. Stainier, and M. Ortiz, 2021: Finite element solver for data-driven finite strain elasticity. *Computer Methods in Applied Mechanics and Engineering*, **379**, 113756, doi:10.1016/j.cma.2021.113756.
URL https://linkinghub.elsevier.com/retrieve/pii/S004578252100092X

[30] Priadi, D., C. Levaillant, L. Penazzi, E. Di Pasquale, and S. Aita, 1991: Introduction of strain rate effects in constitutive equations suitable for sheet metal stamping applications. *MECAMAT 91*, 1991.

[31] Réthoré, J., 2018: *UFreckles, doi:10.5281/zenodo.1433776*.

[32] Rossi, M., M. Badaloni, P. Lava, D. Debruyne, and F. Pierron, 2016: A procedure for specimen optimization applied to material testing in plasticity with the virtual fields method. *AIP Conference Proceedings*, AIP Publishing LLC, 200016.
URL http://aip.scitation.org/doi/abs/10.1063/1.4963634

[33] Rossi, M., P. Lava, F. Pierron, D. Debruyne, and M. Sasso, 2015: Effect of DIC spatial resolution, noise and interpolation error on identification results with the VFM: Effect of DIC spatial resolution, noise and

interpolation on VFM identification. *Strain*, **51**, no. 3, 206–222, doi:10.1111/str.12134.
URL https://onlinelibrary.wiley.com/doi/10.1111/str.12134

[34] Seghir, R. and F. Pierron, 2018: A Novel Image-based Ultrasonic Test to Map Material Mechanical Properties at High Strain-rates. *Experimental Mechanics*, **58**, no. 2, 183–206, doi:10.1007/s11340-017-0329-4.

[35] Stainier, L., A. Leygue, and M. Ortiz, 2019: Model-free data-driven methods in mechanics: material data identification and solvers. *Compututational Mechanics*, **64**, no. 2, 381–393, doi:10.1007/s00466-019-01731-1.
URL http://link.springer.com/10.1007/s00466-019-01731-1

[36] Vinel, A., R. Seghir, J. Berthe, G. Portemont, and J. Réthoré, 2021: Metrological assessment of multi-sensor camera technology for spatially-resolved ultra-high-speed imaging of transient high strain-rate deformation processes. *Strain*, **57**, no. 4, e12381, doi:https://doi.org/10.1111/str.12381.
URL https://onlinelibrary.wiley.com/doi/abs/10.1111/str.12381

[37] Witz, J.-F., P. Lecomte-Grosbras, A. Morch, C. Martel, F. Lesaffre, and M. Brieu, 2017: Digital image correlation for large strain. *International Digital Imaging Correlation Society*, Springer, 163–167.

□